Cell

Structure of the thrombopoietin-MPL receptor complex is a blueprint for biasing hematopoiesis

Graphical abstract

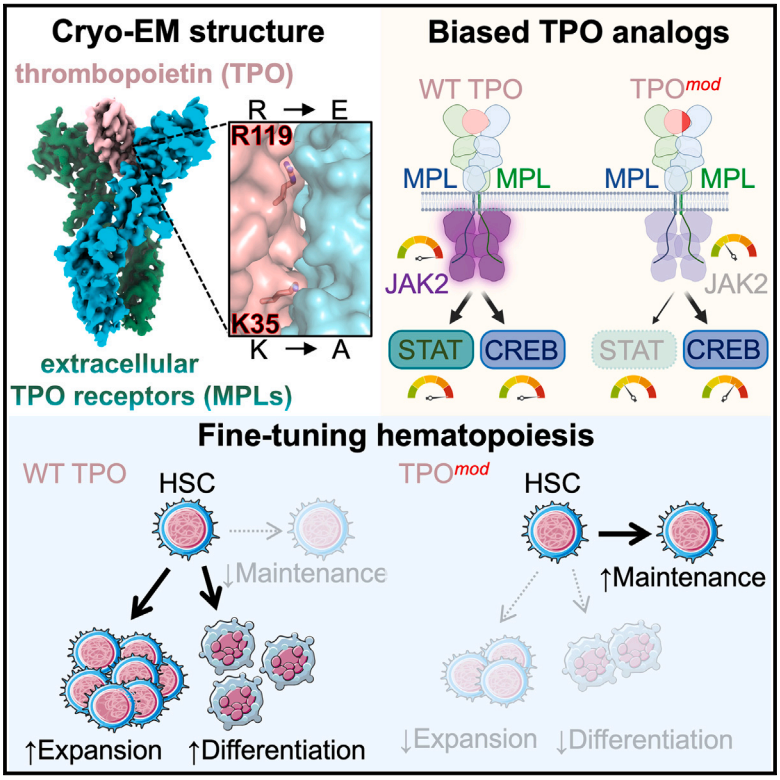

Highlights

- Cryo-EM structure of thrombopoietin-MPL receptor complex at 3.4 Å resolution
- Structure-guided design of thrombopoietin mutants that fine-tune MPL signaling
- Partial agonists decouple functional pleiotropy of thrombopoietin in hematopoiesis

Authors

Naotaka Tsutsumi, Zahra Masoumi, Sophie C. James, ..., Jacob Piehler, Ian S. Hitchcock, K. Christopher Garcia

Correspondence

ntsutsumi@okayama-u.ac.jp (N.T.), ian.hitchcock@york.ac.uk (I.S.H.), kcgarcia@stanford.edu (K.C.G.)

In brief

The thrombopoietin-MPL axis plays essential roles in hematopoietic stem cell biology and platelet production. Cryo-EM structure of the dimeric thrombopoietin-MPL receptor complex enabled design of biased agonists that tune intracellular signaling, thereby uncoupling the primary opposing functions of thrombopoietin signaling, hematopoietic stem cell maintenance, and differentiation.

Tsutsumi et al., 2023, Cell *186*, 1–15
September 14, 2023
https://doi.org/10.1016/j.cell.2023.07.037

CellPress

Cell

CellPress
OPEN ACCESS

Article

Structure of the thrombopoietin-MPL receptor complex is a blueprint for biasing hematopoiesis

Naotaka Tsutsumi,[1,2,3,4,*] Zahra Masoumi,[5] Sophie C. James,[5] Julie A. Tucker,[5] Hauke Winkelmann,[6] William Grey,[5] Lora K. Picton,[1] Lucie Moss,[5] Steven C. Wilson,[1,2] Nathanael A. Caveney,[1,2] Kevin M. Jude,[1,2,3] Cornelius Gati,[2,7] Jacob Piehler,[6] Ian S. Hitchcock,[5,*] and K. Christopher Garcia[1,2,3,8,*]

[1]Department of Molecular and Cellular Physiology, Stanford University School of Medicine, Stanford, CA 94305, USA
[2]Department of Structural Biology, Stanford University School of Medicine, Stanford, CA 94305, USA
[3]Howard Hughes Medical Institute, Stanford University School of Medicine, Stanford, CA 94305, USA
[4]Graduate School of Medicine, Dentistry and Pharmaceutical Sciences, Okayama University, Okayama 700-8530, Japan
[5]York Biomedical Research Institute, Department of Biology, University of York, Heslington, York YO10 5DD, UK
[6]Department of Biology/Chemistry and Center of Cellular Nanoanalytics, Osnabrück University, 49076 Osnabrück, Germany
[7]Biosciences Division, SLAC National Accelerator Laboratory, Menlo Park, CA 94025, USA
[8]Lead contact
*Correspondence: ntsutsumi@okayama-u.ac.jp (N.T.), ian.hitchcock@york.ac.uk (I.S.H.), kcgarcia@stanford.edu (K.C.G.)
https://doi.org/10.1016/j.cell.2023.07.037

SUMMARY

Thrombopoietin (THPO or TPO) is an essential cytokine for hematopoietic stem cell (HSC) maintenance and megakaryocyte differentiation. Here, we report the 3.4 Å resolution cryoelectron microscopy structure of the extracellular TPO-TPO receptor (TpoR or MPL) signaling complex, revealing the basis for homodimeric MPL activation and providing a structural rationalization for genetic loss-of-function thrombocytopenia mutations. The structure guided the engineering of TPO variants (TPO^{mod}) with a spectrum of signaling activities, from neutral antagonists to partial- and super-agonists. Partial agonist TPO^{mod} decoupled JAK/STAT from ERK/AKT/CREB activation, driving a bias for megakaryopoiesis and platelet production without causing significant HSC expansion in mice and showing superior maintenance of human HSCs *in vitro*. These data demonstrate the functional uncoupling of the two primary roles of TPO, highlighting the potential utility of TPO^{mod} in hematology research and clinical HSC transplantation.

INTRODUCTION

Thrombopoietin (THPO or TPO) is a class I cytokine essential for hematopoietic stem cell (HSC) maintenance[1,2] and is the primary driver of megakaryocyte differentiation and platelet production.[3–5] Dysregulation of TPO and the TPO receptor (TpoR or MPL) leads to disease states, with loss-of-function (LOF) mutations leading to thrombocytopenia and bone marrow (BM) failure[6–8] and gain-of-function (GOF) mutations resulting in the development of myeloproliferative neoplasms (MPNs).[9–11] Furthermore, the most common MPN-driver mutations, occurring in JAK2[12,13] and calreticulin,[14,15] cause MPL hyperactivation via interaction with the receptor intracellular and extracellular domains (ECDs), respectively. Clinically, TPO agonists, including the small molecule eltrombopag[16] and the peptibody romiplostim[17] have emerged as key therapies for chronic immune thrombocytopenia (ITP) and severe aplastic anemia.[18,19] However, induction of platelet production comes at the cost of increased HSC proliferation and the risk of BM fibrosis,[20,21] highlighting a critical need to decouple these two functions. Additionally, TPO is one of three key cytokines that are essential for the expansion of functional HSCs *in vitro*[22,23] and is still used today in the majority of new clinical protocols aimed at increasing HSC expansion for transplantation across a range of malignant and non-malignant hematopoietic disorders.[24] Unfortunately, issues remain with TPO-induced HSC proliferation, with TPO dose being critical for optimum HSC output[25] and excessive HSC expansion leading to loss of multilineage regenerative capacity.[26] Thus, balancing TPO-MPL signaling is a critical factor in HSC maintenance and expansion.

The basic activation mechanism, TPO-driven homodimerization of the monomeric MPL chains, was only recently described using single-molecule techniques.[27] Furthermore, GOF mutations in the receptor, calreticulin, and JAK2 all activate MPL by the shared homodimerization mechanism,[27,28] but with a diverse mode of action, activating distinct downstream signaling pathways that, in turn, drive different physiological outcomes, highlighting the plasticity of this pathway.[29] We have previously exploited this diversity in activation by using diabodies that bind to and differentially activate MPL to manipulate functional outcomes,[30] opening up the possibility of developing biased MPL agonists to decouple the functional pleiotropy of MPL.

Although the TPO-MPL-JAK2 axis remains an attractive target for therapeutic intervention, the structure-guided development of agents that fine-tune receptor activation, as seen in other

Please cite this article in press as: Tsutsumi et al., Structure of the thrombopoietin-MPL receptor complex is a blueprint for biasing hematopoiesis, Cell (2023), https://doi.org/10.1016/j.cell.2023.07.037

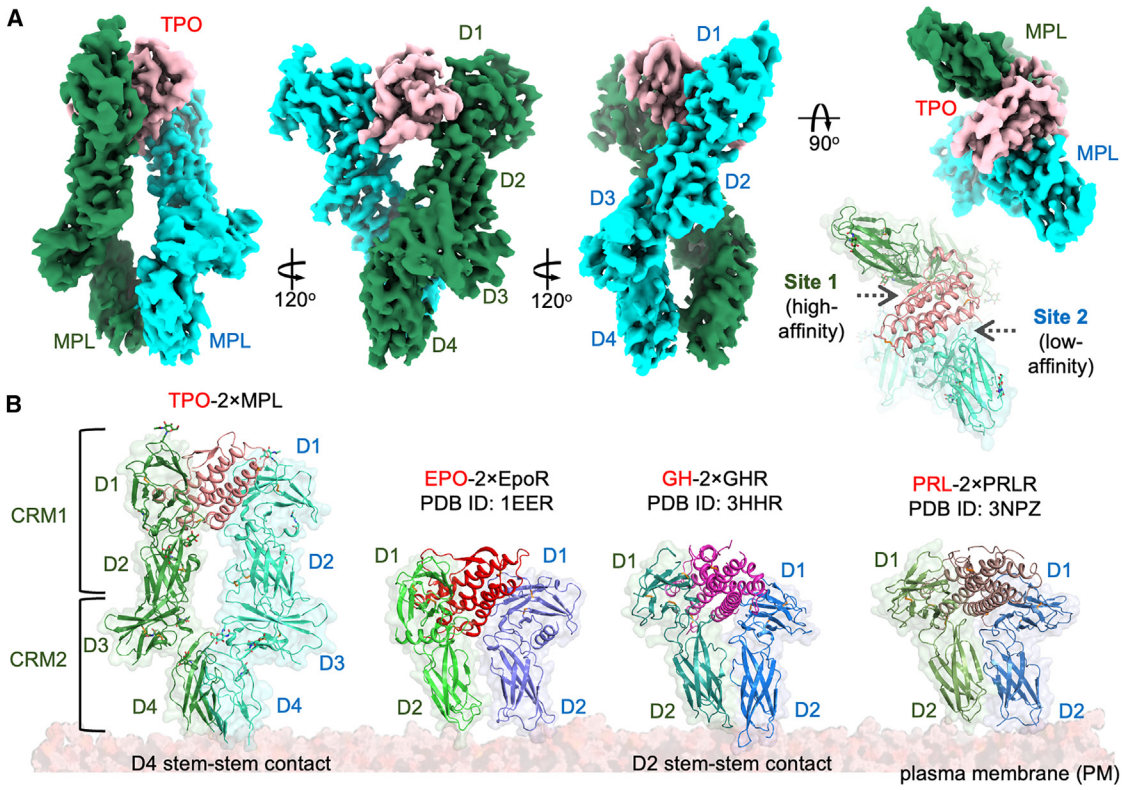

Figure 1. Extracellular structure of the TPO-2×MPL signaling complex

(A) Cryo-EM 3D reconstruction of the TPO-2×MPL_{ECD} complex and ribbon model of the top view covered by a transparent surface. Volumes and cartoons are colored in salmon (TPO), forest green (MPL chain 1), and cyan (MPL chain 2), respectively. The map contour level is set to 9σ.

(B) Comparison of the extracellular domain architectures among MPL, EpoR, GHR, and PRLR. The ligand-receptor complexes are shown side-by-side above a cell membrane cartoon. See also Figure S1.

cytokine receptors and G protein-coupled receptors,[31,32] is hampered by the lack of detailed structural information for the activating TPO-2×MPL complex.

Here, we describe the 3.4 Å cryoelectron microscopy (cryo-EM) structure of TPO bound to two MPL ECDs, in which the cytokine-cytokine receptor interactions are clearly visualized. This provided a blueprint for the design of TPO-based agonists by attenuating the low-affinity interaction site. Intriguingly, we found several biased agonists that stimulated intracellular signaling pathways in a tunable manner and altered cellular outcomes by uncoupling TPO-stimulated HSC expansion and platelet production.

RESULTS

Structure of the TPO-MPL complex

The MPL_{ECD} consists of two cytokine receptor-like modules (CRMs), CRM1 and CRM2, followed by a transmembrane helix (TM) and an intracellular domain (ICD).[33] We co-expressed and purified the functional domain of TPO and the full-length MPL, consisting of the ECD, TM, and unstructured ICD segments (Figures S1A and S1B). Although the TM region was not ordered sufficiently for structure determination in the detergent micelle, 3D reconstruction of the extracellular region visualized the TPO cytokine domain and four globular domains for two MPL chains, D1 and D2 within MPL_{CRM1}, and D3 and D4 within MPL_{CRM2} (Figures 1A and S1C–S1L; Table 1). The MPL structure revealed several unique features (Figure S2A), including tryptophan C-mannosylation[34] at the WSXWS motif-like WGSWS sequence and an extended DE loop (L5) within MPL_{D2} that forms a disulfide bond with MPL_{D3}, constraining the flexibility of the D2D3 module.

MPL_{CRM1} is responsible for TPO recognition, whereas MPL_{CRM2} is critical to bringing receptor TMs and ICDs into close proximity conducive for downstream signal transduction. The 2×MPL_{CRM1} region forms a Y-shaped fork to trap TPO, and the TPO-2×MPL_{CRM1} complex bears a resemblance to the extracellular signaling complexes of the shorter homodimeric cytokine receptor family members sharing a common ancestor[35]; erythropoietin receptor (EpoR),[36,37] growth hormone receptor (GHR),[38] and prolactin receptor (PRLR)[39] contain a single CRM (Figure 1B). However, the dimeric architecture of MPL_{ECD} is more twisted (Figure S2B), with topological features optimal for TPO-induced dimerization. The short N-terminal α helix of the MPL_{ECD} is folded between D1 and D2 (Figure S2A), having the effect of twisting the D2s away from each other and creating a larger D2-D2 distance in the TPO-2×MPL versus EPO-2×EpoR complexes[37] (Figure S2B). These features contrast with the extensive inter-receptor "stem" contacts seen in the GHR and PRLR complexes[38,39] (Figure S2B).

Please cite this article in press as: Tsutsumi et al., Structure of the thrombopoietin-MPL receptor complex is a blueprint for biasing hematopoiesis, Cell (2023), https://doi.org/10.1016/j.cell.2023.07.037

Table 1. Data collection and refinement statistics of the cryo-EM analysis

	hTPO-2×MPL (EMDB-29644, PDB: 8G04)
Data collection and processing	
Nominal magnification	81,000×
Calibrated magnification	46,382×
Voltage (kV)	300
Electron exposure (e/Å^2)	50
Defocus range (μm)	−0.8 to −2.0
Pixel size (Å)	1.078
Symmetry imposed	C1
Initial "particle" images (no.)	9,537,683
Protein particle images (no.)	3,358,637
Final particle images (no.)	329,658
Map resolution (Å)	3.4
FSC threshold	0.143
Map resolution range (Å)	2.8–6.4
Refinement	
Initial model used (PDB code/AF2 code[a])	1V7N, 1EER/AF-P40238-F1
Model resolution (Å)	3.4
FSC threshold	0.5
Map sharpening method	deepEMhanceer (visualization) Phenix LocalAniso (refinement and visualization)[b]
Model composition	
Non-hydrogen atoms	7,314
Protein residues	944
Ligands	12 (6 NAG and 6 MAN)
B factors (Å2)	
Protein	112.12
Ligand	145.92
RMS deviations	
Bond lengths (Å)	0.005
Bond angles (°)	0.608
Validation	
MolProbity score	2.05
Clashscore	7.64
Poor rotamers (%)	0
Ramachandran plot	
Favored (%)	95.31
Allowed (%)	4.69
Disallowed (%)	0
EMRinger score	2.51

[a]AlphaFold2 accession number.
[b]Phenix local anisotropic sharpening based on half maps.

Further, MPL_{D2} is packed against MPL_{D3} with a disulfide bridge (Figure S2A). This disulfide bonding would rigidify the relative orientation of CRM1 and CRM2, possibly playing a role in conveying the ligand-binding geometry to the membrane-proximal region,[40] placing D4s in close proximity for homodimeric MPL activation[27,41,42] (Figure 1A).

TPO bridges two MPL chains via the high- and low-affinity interfaces called site 1 and site 2, fostering TPO-specific binding geometry (Figures 2A, 2B, S2C, and S2D). The interface areas of sites 1 and 2 are ~750 and ~620 Å^2 with shape complementarity scores of 0.652 and 0.598, respectively (Figure 2B). For the high-affinity site 1 interface, the α-helix B′ and the adjacent loop of TPO are jointly recognized by D1 and D2 of MPL. The low-affinity site 2 consists of interfaces between (1) MPL_{D1} and TPO helix C with a unique $R119^{TPO}$:$R102^{MPL}$ stacking[43] and (2) MPL_{D2} and TPO helix A. The LOF thrombocytopenia mutations $R38C/Q^{TPO}$, $R99W^{TPO}$, and $R119C^{TPO}$ are all located at the site 2 interface (Figures 2C and S2D).[33] In a similar manner, the LOF mutant $F104S^{MPL}$ causes thrombocytopenia due to impaired binding to TPO, whereas homozygous $R102P^{MPL}$ mutations alter receptor trafficking, reducing membrane expression and also leading to thrombocytopenia.[33] $F104^{MPL}$ and $R102^{MPL}$ show extensive interactions with TPO at both sites 1 and 2 (Figures 2B, 2C, and S2D). LOF mutations also occur at $W154^{MPL}$ and $R257^{MPL}$, whose sidechains are directed toward the domain core and the mannosylated WGSWS of MPL_{D2}, respectively, stabilizing the protein folding (Figures 2C and S2A).

Structure-guided TPO engineering identifies functional hotspots

TPO activates multiple intracellular signaling pathways via JAK2-mediated receptor phosphorylation and STAT activation in hematopoietic stem and progenitor cells (HSPCs) and cells of the megakaryocyte lineage.[33] In order to probe the molecular determinants of these functional outputs, we exploited the structural information on the low-affinity site 2 interface to design mutants that would alter MPL dimerization to yield differential signaling. We selected five basic residues on the TPO surface that mediate interactions with MPL (Figures 3A top and S3A left). The chosen mutations encompass a range of chemical properties that could affect the interface in different ways,[44] including (1) alanine (small hydrophobic), (2) glutamine (medium polar), (3) histidine (aromatic with positive, maintained charge), and (4) glutamate (negative, opposite charge). In particular, we hypothesized that TPO-R119E and TPO-R119H would be worth querying because $R119^{TPO}$ forms cationic π-π stacking with the counterpart arginine residue (R102) in MPL. Two disease-associated mutants, TPO-R99W and TPO-R119C,[33] were also included, and TPO-K35M was tested to include a hydrophobic residue with similar size to the wild-type (WT) residue.

We then screened side-chain substitutions at each site for their ability to support cell growth using cell-culture-supernatant containing TPO variants (Figures S3A–S3C). Among them, $R31^{TPO}$ variants were mostly non-functional, whereas $R38^{TPO}$ and $R99^{TPO}$ variants all behaved similarly to WT TPO (Figure S3D). $K35^{TPO}$ and $R119^{TPO}$ variants showed the most "tunable" nature, including WT-like, neutral antagonists, partial agonists, and super-agonists (Figure 3B). In cell proliferation assays, TPO-K35A and TPO-K35Q were partial agonists, with TPO-K35Q being less potent compared with TPO-K35A, whereas TPO-K35E did not support cell growth. TPO-R119H

Please cite this article in press as: Tsutsumi et al., Structure of the thrombopoietin-MPL receptor complex is a blueprint for biasing hematopoiesis, Cell (2023), https://doi.org/10.1016/j.cell.2023.07.037

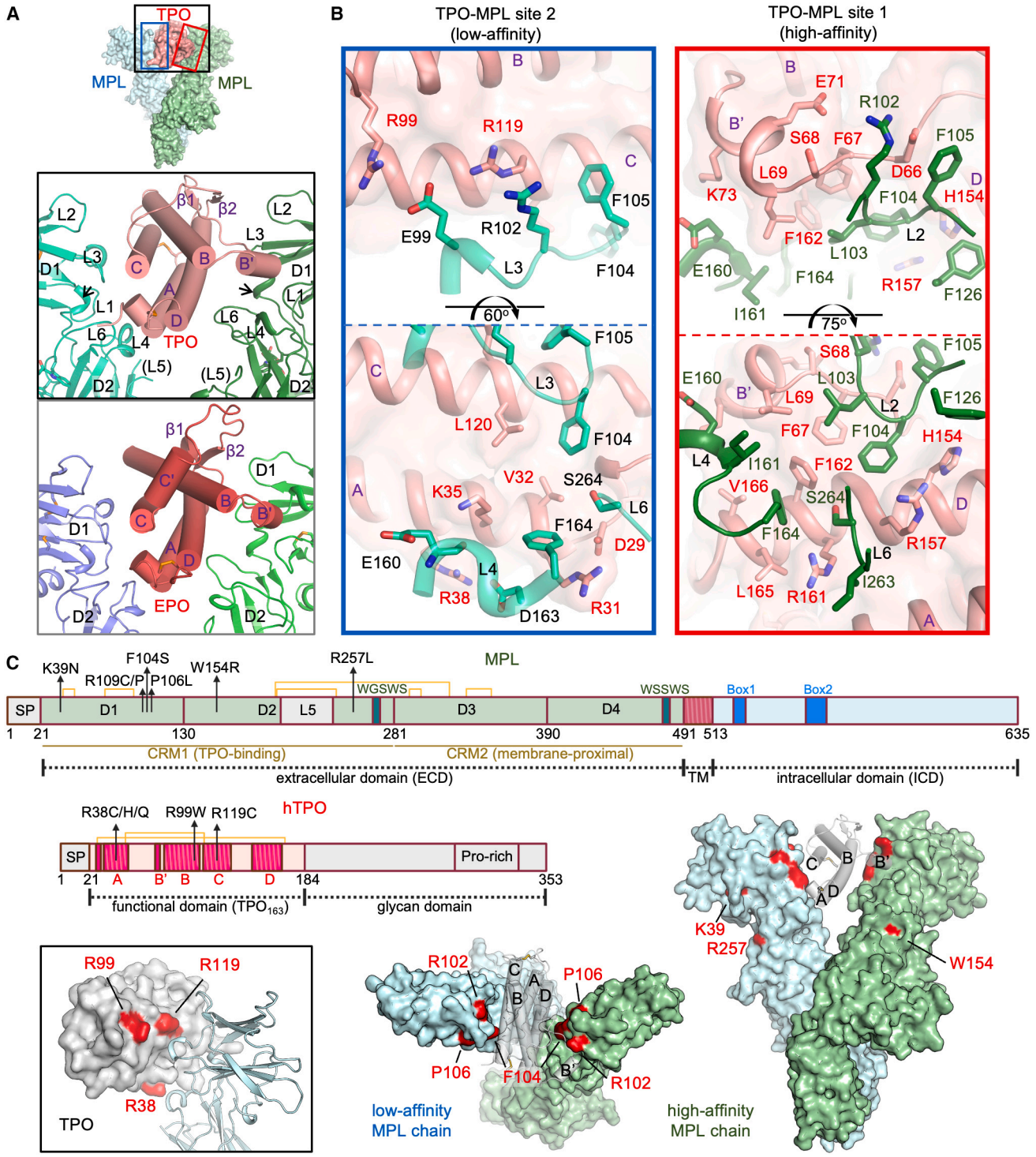

Figure 2. TPO recognition by MPL

(A) Comparison of the cytokine binding mode of the TPO-2×MPL complex with the EPO-2×EpoR complex. The α helices (A–D) are shown as cylinders for TPO (salmon) and EPO (red). Loops 1–6 (L1–L6) of MPL are indicated in the panel, where the extremely long L5 is mostly unresolved in the structure. The black arrows indicate the linker between D1 and D2 of MPL.

(B) Zoomed-in views of the site 2 (blue box) and site 1 (red box) TPO-MPL interfaces. The side chains of the interface residues are shown as sticks and labeled. MPL chains are colored forest green (chain 1) and cyan (chain 2).

(C) Domain diagrams and cartoon representations of TPO and MPL highlighting the LOF mutations. SP, signal peptide, A–D, TPO α helices A–D; Pro-rich, proline-rich region; yellow bracket, disulfide bond in the domain diagrams. LOF single-point mutations are indicated with up arrows in the diagrams and colored in red in the cartoon models. See also Figure S2.

Please cite this article in press as: Tsutsumi et al., Structure of the thrombopoietin-MPL receptor complex is a blueprint for biasing hematopoiesis, Cell (2023), https://doi.org/10.1016/j.cell.2023.07.037

CellPress
OPEN ACCESS

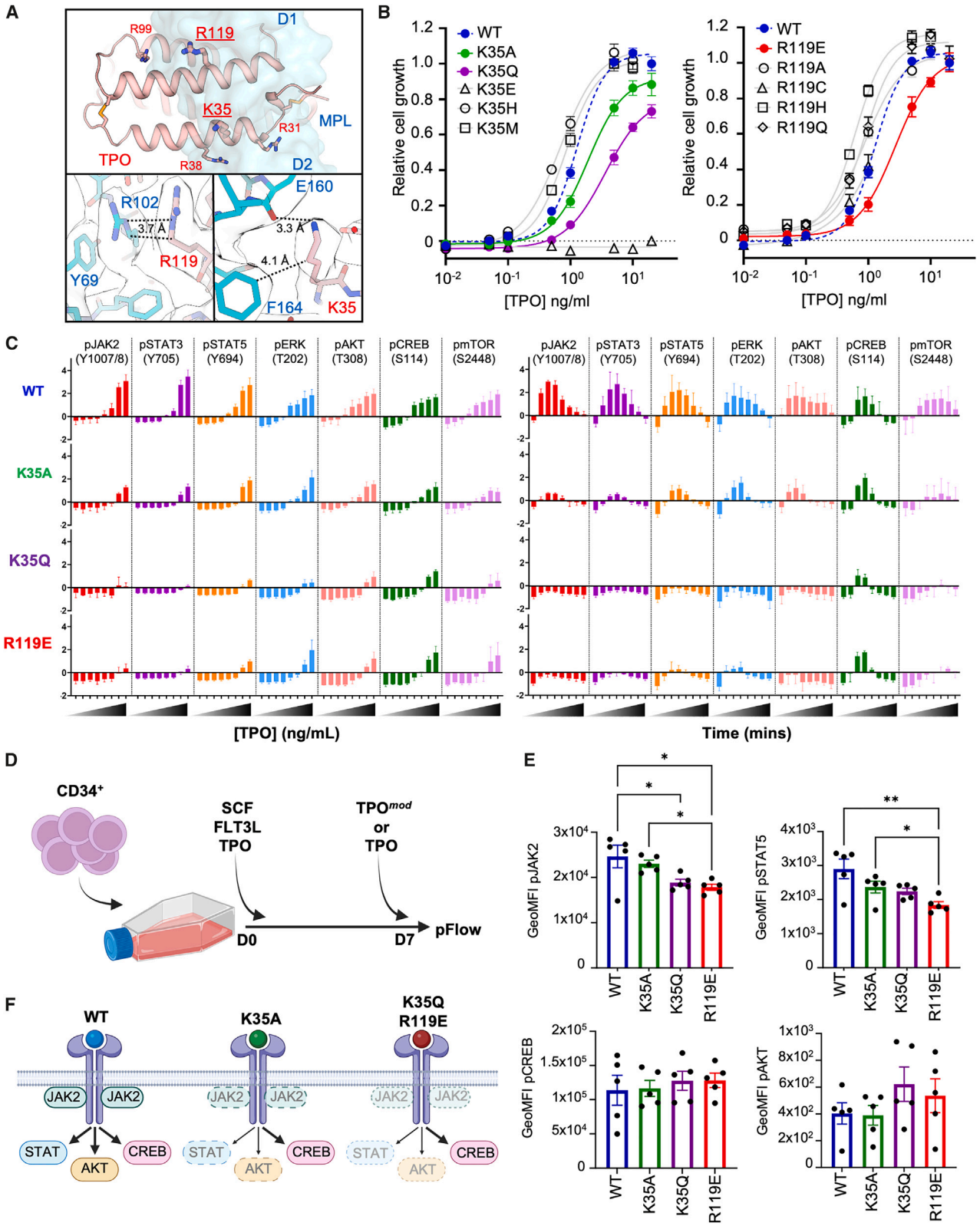

(legend on next page)

Please cite this article in press as: Tsutsumi et al., Structure of the thrombopoietin-MPL receptor complex is a blueprint for biasing hematopoiesis, Cell (2023), https://doi.org/10.1016/j.cell.2023.07.037

appeared to be a more potent agonist than WT TPO, whereas TPO-R119E was a partial agonist (Figure 3B).

We next determined how TPO^{mod} altered signaling using barcoded phosphoflow cytometry in UT7-TPO cells. Signaling was determined by dose (0–100 ng/mL for 30 min) and kinetics (50 ng/mL for 0–240 min). All TPO^{mod} were able to activate signaling (Figures 3C and S4), although maximal stimulation was generally lower than WT TPO, in particular activation of JAK2, STAT3, and STAT5. Of the TPO^{mod} variants, JAK/STAT activation was highest in TPO-K35A, which also exhibited comparable levels of ERK/AKT/CREB activation to WT TPO. Although maximal activation of AKT was comparable to WT TPO, TPO-K35A was not able to maintain activation of AKT for as long as WT TPO. These data are consistent with the finding that levels of phospho-mTOR (S2448), which is phosphorylated by AKT, were lower after treatment with TPO-K35A. Interestingly, TPO-K35Q was less effective than WT TPO at activating all pathways, especially JAK/STAT, although it was able to stimulate CREB activation to a level comparable to TPO-K35A. TPO-R119E shows a similar "fingerprint" to TPO-K35Q, exhibiting low levels of JAK/STAT and ERK/AKT activation while stimulating CREB activation at higher concentrations. Consistent with the proliferation assays, TPO-K35E exhibited neutral antagonism by failing to activate any of the signaling pathways investigated (Figure S4), whereas TPO-R119H activates JAK/STAT more potently than WT TPO, especially at earlier time points (5–30 min; Figure S4).

To enable more precise probing of TPO pharmacology, we purified the WT TPO and selected TPO^{mod}, the partial agonists TPO-K35A/Q and TPO-R119E (Figure S5A). K35^{TPO} Nζ-H forms a hydrogen bond with E160^{MPL} backbone carbonyl, whereas R119^{TPO} makes an arginine-arginine stack with R102^{MPL} and a possible salt bridge with E99^{MPL} (Figures 3A bottom and S2). Surface plasmon resonance (SPR) demonstrated that all the recombinant TPO^{mod} retain the WT site 1 affinity to MPL$_{ECD}$ (Figures S5B and S5C; Table S1), confirming that the proteins are properly folded. These purified TPO^{mod} were then used to determine whether the signaling differences were also observed in human primary HSPCs. Human CD34^{+} cells were expanded with SCF, FLT3L, and TPO for 7 days prior to stimulation with WT TPO or TPO^{mod} for 1 h, and changes in signaling activity were determined by phosphoflow cytometry (Figure 3D). We observed similar trends in the activation of JAK2 and STAT5, with reduced activation in the presence of TPO^{mod}, especially with TPO-R119E, compared with WT TPO (Figure 3E). However, TPO^{mod}-mediated activation of both AKT and CREB was comparable to WT TPO, mirroring the differential signaling observed in the UT7-TPO cell line. Changes in signaling activity are summarized in a schematic (Figure 3F).

We next probed by live cell single-molecule Förster resonance energy transfer (smFRET) how the recombinant TPO^{mod} altered ligand-induced MPL dimerization. To this end, N-terminally ALFA-tagged MPL and C-terminally mEGFP-tagged JAK2 with tyrosine kinase deletion (JAK2ΔTK) were transiently expressed in HeLa cells, and the cell-surface MPL was selectively labeled with ALFA-tag nanobodies conjugated to Cy3B and ATTO643, respectively (Figure 4A). Cells were then stimulated with PBS, 10 nM WT TPO, or 10 nM TPO^{mod}, and MPL dimerization reported via smFRET was quantified by time-lapse total internal fluorescence (TIRF) microscopy with alternated dual-color laser excitation (Figure S6A). Very low levels of unstimulated MPL dimerization and strong dimerization by WT TPO were confirmed by smFRET (Figures 4B and 4C; Video S1). The mean FRET efficiency of 32% observed for WT TPO-induced MPL dimers was consistent with the ~7.2 nm distance between the MPL N termini observed in the structure (Figure 4D). All three TPO^{mod} induced significantly lower levels of MPL dimerization than WT TPO (Figures 4C and S6B; Video S1), in line with an attenuated site 2 interaction affecting the monomer-dimer equilibrium. Although differences among different TPO^{mod} were minor, lower dimerization by TPO-R119E compared with TPO-K35A was statistically significant. Because the geometry of cytokine receptor dimers has been shown to influence signaling,[45] we used FRET to gauge the effects of TPO^{mod} versus WT TPO. No significant differences in the FRET efficiencies were observed among the TPO variants (Figure 4D; Video S2), confirming that the MPL dimer geometries were not affected by the TPO mutations and that the signaling effects are instead due to differences in the second MPL chain binding efficiency. Consistently, more frequent association and dissociation of MPL dimers was observed for TPO^{mod} compared with WT TPO (Videos S3 and S4). We also reproduced the same experiments in the presence of C-terminally mEGFP-tagged

Figure 3. Tuning the TPO-MPL site 2 interaction

(A) Functional determinants of the TPO-MPL site 2 interface. (Top) TPO is shown as a pink ribbon, and MPL is shown as cyan transparent surface representation. The five TPO residues selected for the initial mutagenesis screening, including two tunable ones, K35^{TPO} and R119^{TPO}, subjected to further signaling and functional characterization, are shown as sticks. (Bottom) Close-up views of K35^{TPO} and R119^{TPO} interacting with MPL. The cryo-EM map is shown as a gray transparent surface and overlaid on the structure at a contour level of 10σ.

(B) UT7-TPO viability assays comparing treatment with increasing concentrations of WT TPO or TPO^{mod} supernatant for 72 h. Data presented as relative mean cell growth (±SEM) compared with maximal stimulation with WT TPO.

(C) Signaling activity was determined by cell barcoded phosphoflow cytometry with either increasing concentrations of WT TPO or TPO^{mod} (0–100 ng/mL for 30 min, left) or increasing time (50 ng/mL, 0–240 min, right). Data were normalized by generating a *Z* score of the mean from four independent experiments (±SEM).

(D) Schematic outlining the *in vitro* method used to expand human CD34^{+} cells in 7-day culture followed by TPO stimulation and phosphoflow cytometry to determine signaling response.

(E) Intracellular signaling was determined in EPCR^{+} HSCs re-treated with TPO on day 7 for 1 h and stained for pJAK2 (Y1007 + Y1008), pSTAT5(Y694), pCREB(S133), and pAKT(S473). For all human HSC signaling graphs, a one-way ANOVA with post hoc Kruskal-Wallis test was used to calculate significance of differences. *$p < 0.05$, **$p < 0.005$.

(F) Schematic summarizing the changes in signal activation comparing WT TPO and TPO^{mod}. Arrow thickness represents relative level of signaling. See also Figures S3–S5.

Please cite this article in press as: Tsutsumi et al., Structure of the thrombopoietin-MPL receptor complex is a blueprint for biasing hematopoiesis, Cell (2023), https://doi.org/10.1016/j.cell.2023.07.037

CellPress
OPEN ACCESS

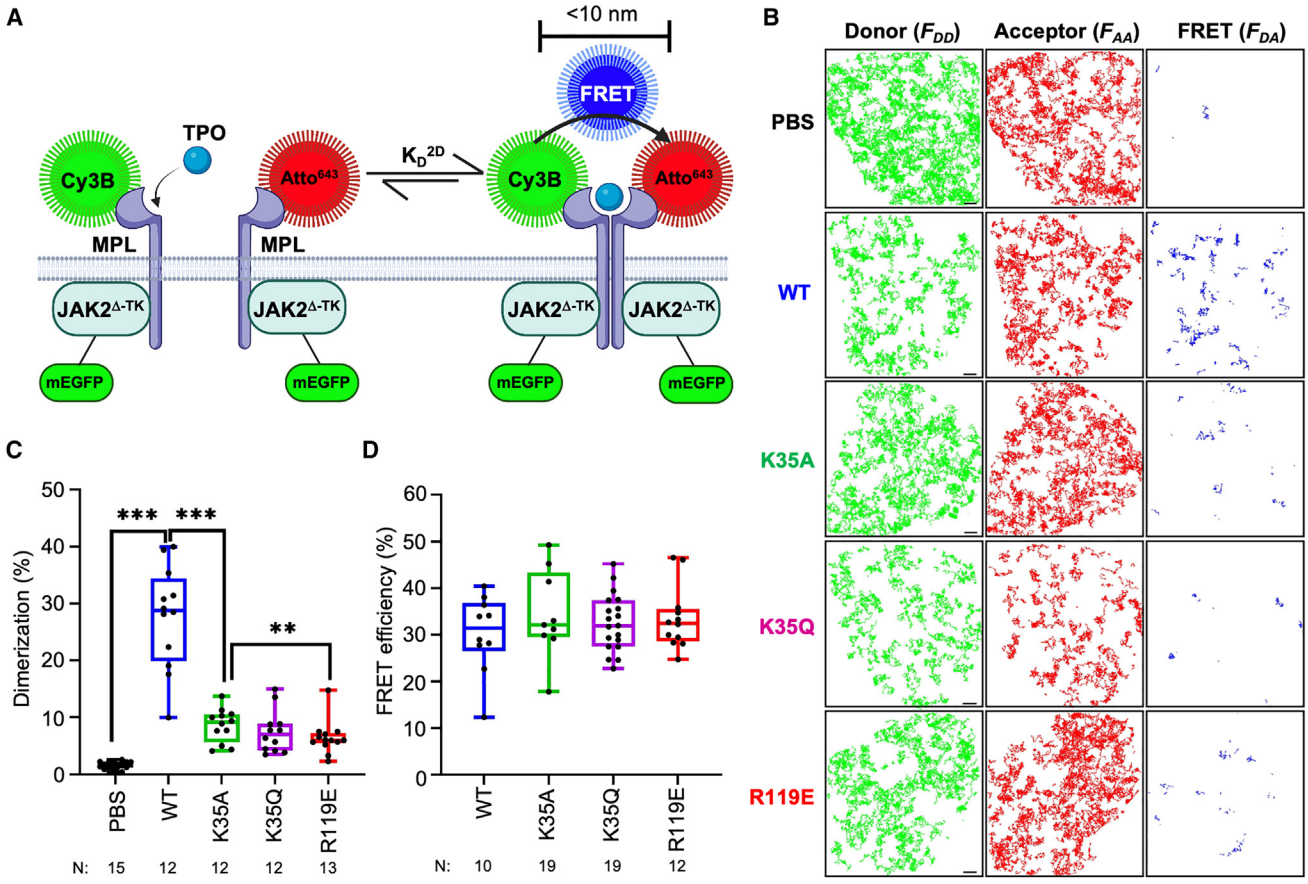

Figure 4. Quantifying the MPL monomer-dimer equilibrium by single-molecule FRET (smFRET)

(A) Schematic illustration of the method used to determine MPL monomer-dimer equilibrium. Labeling of ALFA-tagged MPL by anti-ALFA nanobodies site-specifically conjugated with Cy3B and ATTO643, respectively. JAK2ΔTK was used to observe MPL dimerization in a more physiological setting, whereas JAK2ΔPKΔTK was used to assess the relative lifetime of the TPO-induced receptor dimers without stabilization by the JAK2 PK-PK interaction, enabling indirect comparison of the site 2 affinities among WT TPO and TPO^{mod}.

(B) Representative trajectory maps of Cy3B-labeled MPL-JAK2ΔTK upon donor excitation in green ("Donor") of ATTO643-labeled MPL-JAK2ΔTK upon direct acceptor excitation in red ("Acceptor") and sensitized acceptor fluorescence upon donor excitation in blue ("FRET"), probed in the presence of 10 nM WT TPO or TPO^{mod}. Scale bars: 2 μm.

(C) Quantification of MPL-JAK2ΔTK homodimerization in the presence of 10 nM WT TPO or TPO^{mod}. Each data point represents the analysis from one cell with the number (N) of cells measured for each condition indicated.

(D) smFRET efficiencies in MPL-JAK2ΔTK homodimers observed in the presence WT TPO or TPO^{mod}. Each data point represents the analysis from one trajectory with the number (N) of trajectories measured for each condition indicated. Data in (C) and (D) are presented as box plots and indicate the data distribution of 2nd and 3rd quartile (box), median (line), and minimum and maximum values (whiskers). Significances were determined using the two-sample Kolmogorov-Smirnov test in MATLAB. **p ≤ 0.01, ***p ≤ 0.001. See also Figures S5 and S6.

JAK2 with deletions of tyrosine kinase and pseudokinase domains (JAK2ΔPKΔTK) where the receptor dimers were not further stabilized by JAK2 PK-PK interactions[41] (Figures S6C–S6E), enabling semi-quantitative estimation of the apparent dimer lifetime of 0.88 s for WT TPO, 0.51 s for TPO-K35A, 0.37 s for TPO-K35Q, and not determined (shorter than TPO-35Q) for TPO-R119E.

TPO^{mod} variants stimulate platelet production while preserving HSCs in mice

Because TPO is essential for both HSC maintenance and megakaryocyte differentiation,[1–5] we next determined whether TPO^{mod} altered hematopoiesis *in vivo*. TPO and MPL sequences, including K35^{TPO} and R119^{TPO}, are highly conserved in human and mouse, allowing us to generate equivalent TPO^{mod} mutations in murine TPO (mTPO^{mod}) and purify the recombinant proteins (Figure S5A). To characterize the biological effect and function of mTPO^{mod} *in vivo*, mice were treated with PBS or 5 μg recombinant mTPO (WT or mTPO^{mod}) daily for 5 days, taking complete blood counts at days 5, 7, 10, and 14 (Figure 5A). For BM analysis, mice were euthanized at day 7 (Figure 5A) because this was the time point at which maximal hematological impact was observed. WT mTPO induced a significant expansion of EPCR^{+} long-term (LT)-HSCs and increased numbers of BM CD41^{+} megakaryocyte progenitors (MKPs) compared with PBS at day 7 (Figures 5B and 5C). In comparison, although

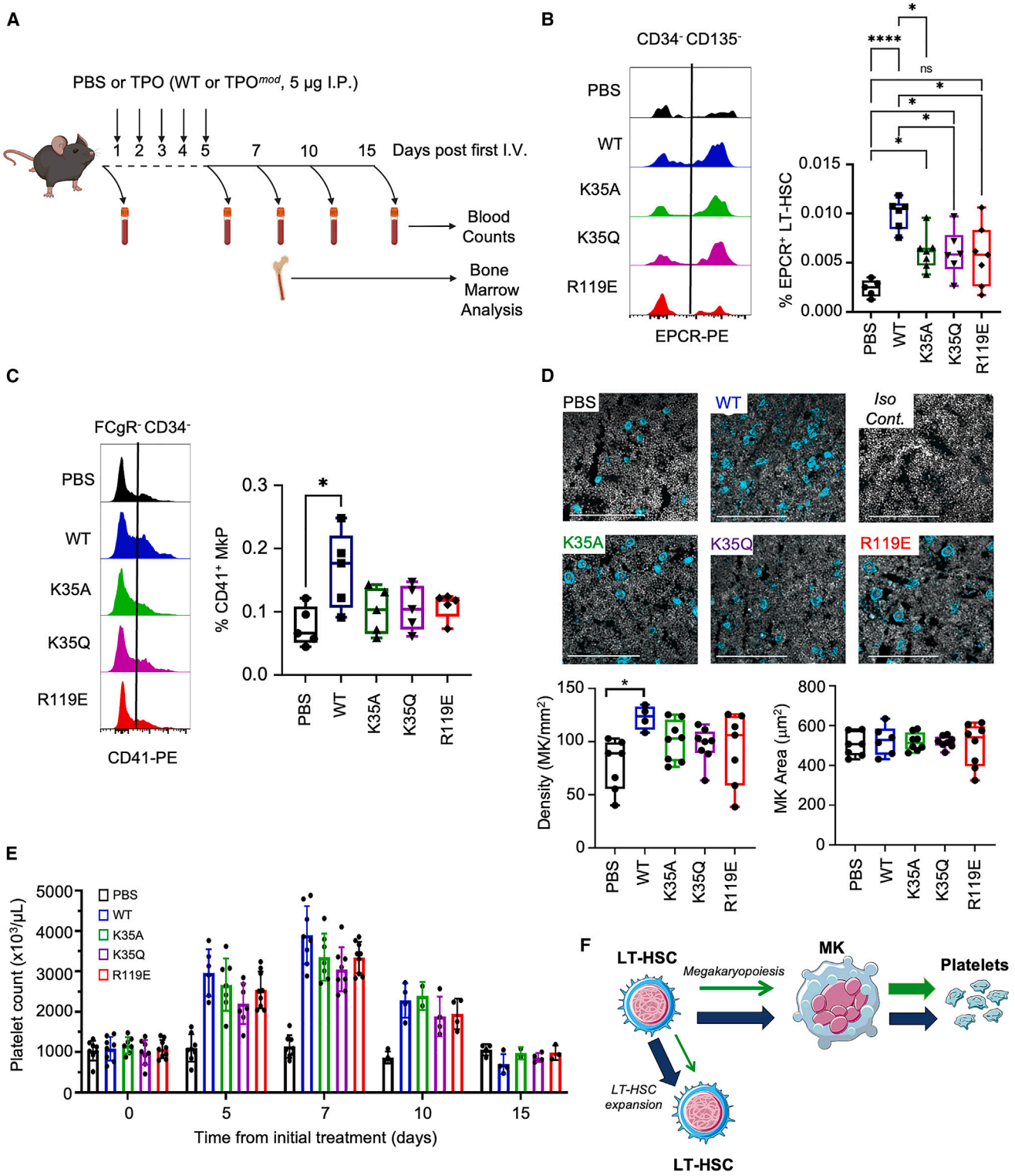

Figure 5. Functional effects of TPO^{mod} on murine hematopoiesis *in vivo*

(A) Schematic of the experimental workflow for *in vivo* murine TPO functional analysis.

(B) (Left) representative histogram of EPCR$^+$ HSCs in the HSPC (LSK CD34$^-$CD135$^-$) compartment and (right) frequency of EPCR$^+$ LT-HSCs in the bone marrow of mice treated with PBS, WT mTPO, or mTPO^{mod} at day 7 (n = 5 from three independent experiments).

(legend continued on next page)

mTPO^{mod} did increase the number of EPCR$^+$ LT-HSCs compared with PBS, the expansion was reduced compared with WT mTPO (Figure 5B), and we observed no significant change in the number of MKPs with mTPO^{mod} compared with PBS (Figure 5C). To determine whether the difference in MKPs was also observed in mature MKs, day 7 BM was sectioned and the number and size of CD41$^+$ MKs quantified (Figure 5D). Only WT mTPO treatment significantly increased the number of BM MKs compared with PBS, whereas the overall size of BM MKs was not altered by mTPO treatment. WT mTPO and mTPO^{mod} increased circulating platelet counts to a similar extent compared with PBS, peaking at day 7 and returning to normal levels by day 15 (Figure 5E). All other circulating blood lineages were unchanged. Taken together, these data demonstrate that modification of TPO uncouples platelet production *in vivo* from HSC and progenitor expansion (Figure 5F).

TPO^{mod} variants preserve human HSCs during *in vitro* expansion

State-of-the-art human *ex vivo* HSC expansion for transplantation currently relies on supplementation with TPO[46] or TPO mimetics.[47] Without the addition of supplementary molecules, human HSCs reach near-exhaustion over 7 days of culture due to rapid stimulation and expansion.[48] Encouraged by the effect of TPO^{mod} on murine HSCs *in vivo*, we tested their ability to maintain human HSCs *ex vivo* (Figure 6A). In our culture conditions, WT TPO led to a greater expansion and differentiation of all cells, of which only a small proportion were EPCR$^+$ HSCs, suggesting HSC exhaustion (Figure 6B). However, substituting WT TPO with TPO^{mod} significantly diminished total cell count by day 7, whereas the proportion of EPCR$^+$ HSCs was significantly increased, particularly with TPO-K35A (Figure 6B). This suggested improved preservation of the HSCs *in vitro* at the expense of cell proliferation, implying a potential uncoupling of proliferation/differentiation from stem cell maintenance by TPO^{mod}.

To assess the functional impact of TPO variants, colony formation assays were performed following 7 days of CD34$^+$ cell expansion. After 14 days of differentiation, total colony count, representing the proportion of colony-forming units in the initiating population, was significantly higher in cultures from cells expanded with TPO-K35A (Figure 6C). However, the frequency of colony types was not different between the groups, suggesting that expansion with TPO variants did not skew cell differentiation potential.

We further studied the transcriptome of primitive cells (CD34$^+$ CD45RA$^-$) in our culture conditions at single-cell resolution (Figure S7A). We identified similar profiles of differentiation trajectory (Figures S7B and S7C) and cellular subtypes (Figures S7D and S7E), which led to few differentially expressed genes in pseudobulk total cells between TPO^{mod} and WT TPO controls (Figures S7F and S7G). Focusing on HSCs characterized by *HLF* expression[49] (Figures 6D and S7E), we noted a strong overlap between WT TPO and TPO^{mod} in differentially expressed genes in *HLF*-positive versus *HLF*-negative HSCs (Figures 6E and S7F). The *HLF*-positive HSC populations showed few differentially expressed genes when comparing WT TPO and TPO^{mod} treatments, with the least overlap between TPO-K35Q and TPO-R119E (Figure 6F), of which a large proportion were downregulated ribosomal genes, in line with lower activation of HSCs compared with WT TPO. These data suggest that, although WT TPO drives greater total expansion of HSCs and progenitor cells, TPO^{mod} maintains primitive HSCs without leading to excessive proliferation and differentiation of progenitor cells (Figure 6G).

DISCUSSION

TPO is essential for normal hematopoiesis, governing key processes from HSC maintenance and proliferation to myeloid differentiation and platelet production.[50–52] Here, the structure of the active TPO-2×MPL extracellular complex enabled us to apply protein engineering approaches to modify TPO to promote certain signaling outcomes and regulate TPO pleiotropy.[31] We modified TPO at two residues in the site 2 interface to generate three TPO^{mod} (TPO-K35A, TPO-K35Q, and TPO-R119E) and thus create functionally biased analogs. In comparison to other synthetic TPO agonists, TPO^{mod} are unique in that they are predicted to maintain the normal binding geometry of the dimeric receptor, which has been shown to be a key determinant of signaling outcome,[45] while showing differential efficacies in MPL-JAK2 dimer formation compared with the endogenous complex.[31,45] The synchronized changes in JAK/STAT activation and cell growth in UT7-TPO cells confirmed the ability of TPO^{mod} to differentially regulate cytokine-induced proliferation via the JAK/STAT signaling pathway. Interestingly, however, attenuation of JAK2 and STAT3/5 phosphorylation was not necessarily coupled to changes in the phosphorylation of other downstream effectors, such as AKT and CREB, and differed among TPO^{mod}. Because the high-affinity site 1 interaction of TPO with MPL is maintained, the changes in signaling and cell growth are not a result of an overall reduction in TPO binding to target cells. Likewise, the geometry of MPL dimers is not affected by TPO^{mod} as confirmed by the unaltered FRET efficiencies. Thus, differences in the maximum number and/or lifetime of the MPL dimers formed by TPO^{mod} compared with WT TPO likely confers selective signaling in TPO-responsive cells.

(C) (Left) representative histogram of CD41$^+$ megakaryocyte progenitors (MKP) within the megakaryocyte-erythroid progenitor (Lin$^-$ cKit$^+$ Sca1$^-$ CD16/32$^-$ CD34$^-$) compartment and (right) frequency of MKPs in the bone marrow of mice treated with WT mTPO or mTPO^{mod} (n = 5 from three independent experiments).
(D) Enumeration of CD41$^+$ BM MKs at day 7 post PBS, WT mTPO, and TPO^{mod} treatment (CD41, cyan; nuclear staining [DAPI], white). Whole femur sections were analyzed using a fully automated Axio Scan.Z1 slide scanner (top) and positive staining was quantified using StrataQuest software (bottom). Scale bars: 200 μm.
(E) Circulating platelet counts following treatment with PBS, WT mTPO or mTPO^{mod}. Each data point represents mean count ± SEM of at least seven mice (range 7–9) for days 0–7 and at least two mice (range 2–4) on days 10–15 from four independent experiments.
(F) Schematic summarizing the effects of WT TPO and TPO^{mod} on LT-HSC expansion and megakaryopoiesis *in vivo*.
A one-way ANOVA with post hoc Kruskal-Wallis (B and C) or Tukey's (D) tests was used to calculate significance of differences where *$p < 0.05$, ****$p < 0.0001$; ns, not significant. See also Figure S5.

Please cite this article in press as: Tsutsumi et al., Structure of the thrombopoietin-MPL receptor complex is a blueprint for biasing hematopoiesis, Cell (2023), https://doi.org/10.1016/j.cell.2023.07.037

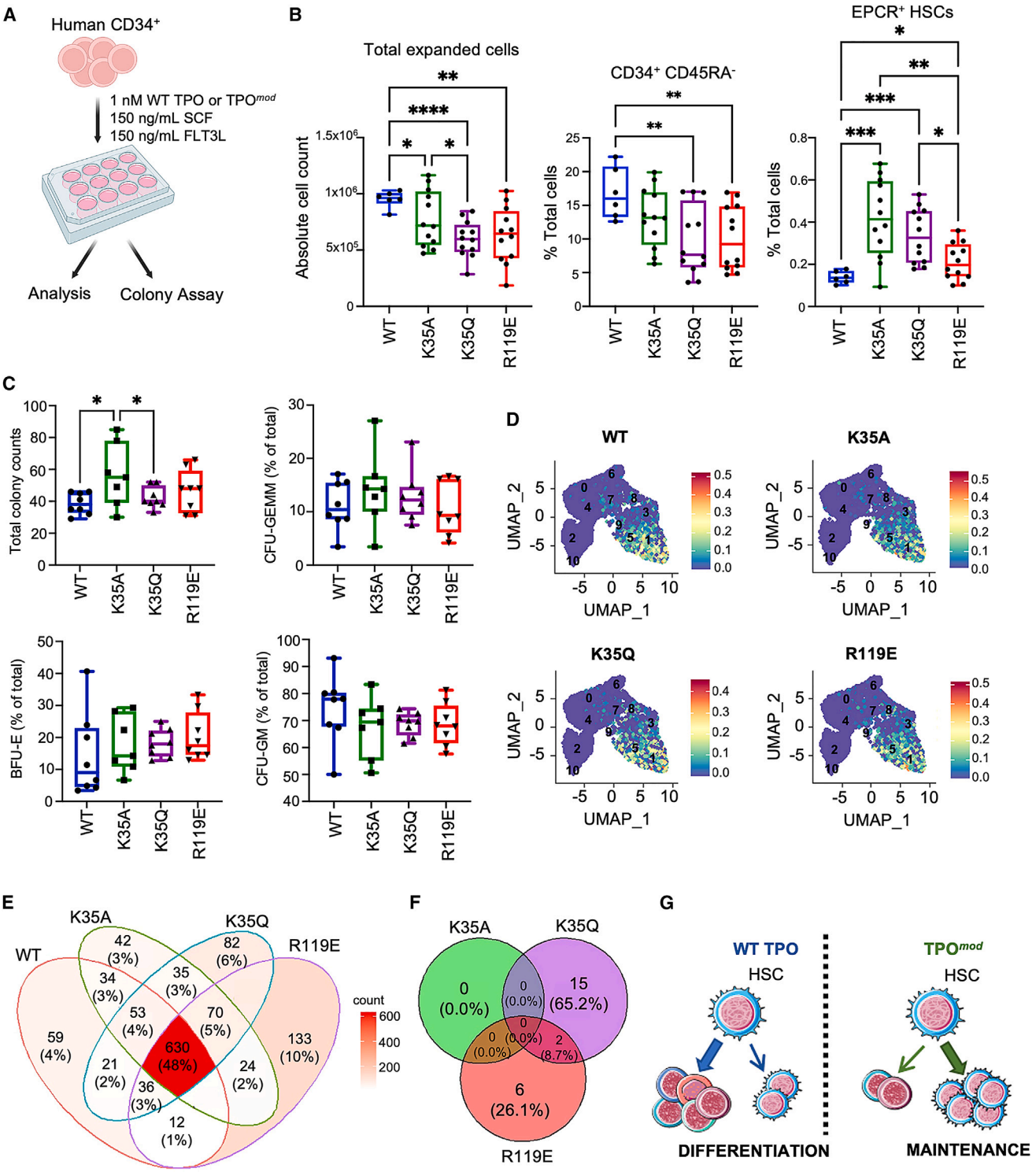

Figure 6. Functional effects of TPO^{mod} on human HSCs *in vitro*

(A) Schematic of the experimental workflow for *in vitro* human TPO functional analysis using human CD34$^+$ cells in 7-day expansion cultures.

(B) Quantification of total cell expansion after 7 days and frequency of primitive progenitors (CD34$^+$ CD45RA$^-$) and CD90$^+$ EPCR$^+$ HSCs in human CD34$^+$ cultures treated with WT TPO or TPO^{mod}.

(C) Colony count and frequency from the colony-forming unit assays generated from 200-cell input following a 7-day expansion of CD34$^+$ cells in the presence of TPO variants.

(legend continued on next page)

Please cite this article in press as: Tsutsumi et al., Structure of the thrombopoietin-MPL receptor complex is a blueprint for biasing hematopoiesis, Cell (2023), https://doi.org/10.1016/j.cell.2023.07.037

The clinical use of TPO receptor agonists (TPO-RAs) for chronic ITP[18,19] and severe aplastic anemia is now well established. However, the currently available TPO-RAs can act as a double-edged sword, in part due to their impact on various levels of the hematopoietic hierarchy. One example is the development of morphologically abnormal MKs in response to TPO-RA treatment, including MKs with hyperlobulated nuclei and MK clustering, both of which are hallmarks of MK development in essential thrombocythemia.[53] Therefore, the ability to fine-tune TPO signaling to specifically increase platelet count in ITP patients without impacting progenitor expansion or normal MK differentiation would be clinically attractive. *In vivo* mouse platelet response to mTPO^{mod} treatment was similar to WT mTPO; however, HSC, MKP, and MK expansion in the BM were lower for mTPO^{mod} than WT mTPO. These results indicated that mTPO^{mod} could increase platelet production by MKs while limiting excessive stem and progenitor cell and MK expansion, thus providing a route to precision targeting of MPL.

TPO is also critical for both murine and human HSC maintenance and expansion *ex vivo*,[54] and there is increasing evidence that TPO dose may play a major role in stem cell production *in vitro*.[25] Over 7 days of *in vitro* culture in the presence of WT TPO, HSCs exhaust to near complete depletion without additional cytokine treatment.[25] Similar to our observations in mice, the overall level of proliferation in human HSPC cultures was significantly lower with TPO-K35A/Q and TPO-R119E treatment, which, in turn, preserved a higher frequency of EPCR$^+$ HSCs. Examination of the transcriptome of TPO^{mod}-expanded HSCs demonstrated high levels of similarity to WT TPO-expanded HSCs, suggesting that these cells are not compromised and highlighting potential for the application of TPO^{mod} in tuning functional outcomes in regenerative medicine. The ability to tune TPO signaling activity by altering how the cytokine interacts with its receptor raises the exciting possibility of improving standard *in vitro* HSC expansion protocols for allogeneic transplantation. Indeed, the need to stimulate HSCs for gene therapy can itself reduce the stem cell pool pre-transplantation, and there are major efforts underway to preserve more HSCs during gene therapy protocols.[55] BM transplantation was the first regenerative medicine approach to enter the clinic, and protocols for expansion of HSCs (the LT source of reconstitution) have largely remained unchanged.[56] Newer protocols aimed at expanding HSCs from umbilical cord blood have shown promise[57,58] but still rely on WT TPO supplementation and are thus balancing proliferation with loss of LT reconstitution potential in basal conditions. The ability to direct TPO-MPL signaling to support new expansion protocols offers much promise for the future of HSC transplantation.

Taken together, our data demonstrate that TPO, a master regulator of hematopoiesis, is a tunable cytokine. We used the structure of the signaling extracellular TPO-2×MPL complex to design TPO^{mod} that differentially controls cellular outcomes. Considering the therapeutic importance of TPO and TPO mimetics, our findings provide the basis for an opportunity to explore MPL signaling at a detailed molecular level and to develop selective TPO^{mod} with clinical potential.

Limitations of the study

Although TPO^{mod} induced intriguing signaling and functional outputs *ex vivo*, xenograft transplantation assays would be beneficial to assess the longer-term self-renewal and multilineage potential of HSCs expanded by TPO^{mod} administration. We demonstrated that the unique functional outcomes of TPO^{mod} stimulation are due to biased cell signaling through attenuated interaction between TPO and the low-affinity, secondary MPL chain required for homodimeric receptor activation. However, quantitative analysis of the site 2 interaction for each TPO^{mod}, which are hampered by technical difficulties, would be required for mechanistic interpretation of the functional data.

STAR★METHODS

Detailed methods are provided in the online version of this paper and include the following:

- KEY RESOURCES TABLE
- RESOURCE AVAILABILITY
  - Lead contact
  - Materials availability
  - Data and code availability
- EXPERIMENTAL MODEL AND STUDY PARTICIPANT DETAILS
  - Mammalian cell lines and culture conditions
  - Insect cell lines and culture conditions
  - Murine models
- METHOD DETAILS
  - Preparation of the ligand-receptor complex for structural study
  - Cryo-EM sample preparation and data acquisition
  - Cryo-EM data processing
  - Model building and refinement
  - Preparation and quantitation of TPO variants for screening by cell proliferation and signaling assays
  - Cell Proliferation assays
  - Multiplex fluorescent barcoding and phospho-flow cytometry
  - Purification of TPO variants for signaling and functional analyses
  - Surface Plasmon Resonance Analysis

(D) Dimensionality reduction of WT and TPO^{mod} single-cell (sc)RNA sequences from CD34$^+$ CD45RA$^-$ cells after 7 days of expansion *in vitro*. HSC heatmap statistic is mapped based on phenotypic HSC genes (positive: CD34, THY1, PROCR, HLF, AVP, MLLT3, SPINK2, PROM1, FLT3, HOXA9, and MECOM; negative: FLI1, GATA1, HBD, and ITGA2B).
(E) Venn overlap of *HLF*$^+$ vs. *HLF*$^-$ differentially expressed genes for each TPO treatment.
(F) Venn overlap of differentially expressed genes between WT and TPO^{mod} *HLF*$^+$ HSCs.
(G) Schematic summarizing the effects of WT TPO and TPO^{mod} on *ex vivo* human HSC expansion.
A one-way ANOVA with post hoc Kruskal-Wallis tests was used to calculate significance of differences where *$p < 0.05$, **$p < 0.005$, ***$p < 0.0005$, ****$p < 0.0001$. See also Figure S7.

- Mouse TPO treatment
- Flow cytometry analysis of hematopoietic stem cells (HSCs) and megakaryocyte progenitors (MKPs) in mouse bone marrow
- Histological analysis of mouse bone marrow
- Umbilical cord blood (UCB) CD34 cell culture and signaling
- Single cell RNA sequencing library preparation
- Single molecule fluorescence imaging and analysis

● QUANTIFICATION AND STATISTICAL ANALYSIS

SUPPLEMENTAL INFORMATION

Supplemental information can be found online at https://doi.org/10.1016/j.cell.2023.07.037.

ACKNOWLEDGMENTS

The cryo-EM data were collected at the Cryo-EM facility at the HHMI Janelia Research Campus. We thank Drs. Zhiheng Yu, Rui Yan, and Doreen Mathies for their support in microscope operation. Cryo-EM data processing was performed on the Sherlock cluster. We thank Stanford University and the Stanford Research Computing Facility for maintaining computational resources. Preliminary cryo-EM screening was performed at the Stanford cryo-EM center (cEMc). We thank Drs. Dong-Hua Chen and Elizabeth Montabana for their support in operating the facilities and providing user training and support. We thank Andrew Leech (Molecular Interactions Laboratory of the University of York Bioscience Technology Facility) and Claire Shepherd (Cytiva) for assistance with generating the SPR data; Gillian Goodwin (Cytiva) for assistance with SPR figure preparation; and Karen Hogg and Graeme Park (Imaging and Cytometry Laboratory of the University of York Bioscience Technology Facility) for assistance with phosphoflow cytometry, cell sorting, and imaging. We thank Sally James and Lesley Gilbert for preparation of 10x sequencing libraries and Alastair Droop and Sandy Macdonald for analytic support (York Bioscience Technology Facility & Data Sciences Team). We also thank the Biology Services Facility (University of York) for assisting with mouse experiments. K.C.G. is an investigator of the Howard Hughes Medical Institute and the Younger Family Chair and is supported by NIH funding (R37AI051321), the Ludwig Institute, and Emerson Collective. I.S.H. is supported by funding from Cancer Research UK (A24593) and Blood Cancer UK (22001). J.P. is supported by the DFG (PI 405/15-2 – 326558201). W.G. is supported by funding from the Medical Research Council (MR/X007146/1) and the Children's Cancer and Leukaemia Group (CCLGA 2022 13 Grey).

AUTHOR CONTRIBUTIONS

Conceptualization, N.T. and K.C.G.; methodology, N.T., J.A.T., W.G., J.P., I.S.H., and K.C.G.; investigation, N.T., Z.M., S.C.J., J.A.T., H.W., W.G., L.K.P., L.M., S.C.W., N.A.C., K.M.J., I.S.H., and C.G.; funding acquisition, J.P., W.G., I.S.H., and K.C.G.; project administration, I.S.H. and K.C.G.; supervision: I.S.H. and K.C.G.; writing – original draft, N.T., Z.M., J.A.T., W.G., I.S.H., and K.C.G.; writing – review & editing, all authors.

DECLARATION OF INTERESTS

K.C.G., N.T., and I.S.H. are inventors on a United States provisional patent (63/519,687, filed 15 August 2023) related to the mutant TPO molecules described in the manuscript.

Received: February 15, 2023
Revised: June 26, 2023
Accepted: July 28, 2023
Published: August 25, 2023

REFERENCES

1. Alexander, W.S., Roberts, A.W., Nicola, N.A., Li, R., and Metcalf, D. (1996). Deficiencies in progenitor cells of multiple hematopoietic lineages and defective megakaryocytopoiesis in mice lacking the thrombopoietic receptor c-Mpl. Blood *87*, 2162–2170. https://doi.org/10.1182/blood.v87.6.2162.bloodjournal8762162.

2. Carver-Moore, K., Broxmeyer, H.E., Luoh, S.M., Cooper, S., Peng, J., Burstein, S.A., Moore, M.W., and De Sauvage, F.J. (1996). Low levels of erythroid and myeloid progenitors in thrombopoietin- and c-mpl-deficient mice. Blood *88*, 803–808. https://doi.org/10.1182/blood.v88.3.803.803.

3. Lok, S., Kaushansky, K., Holly, R.D., Kuijper, J.L., Lofton-Day, C.E., Oort, P.J., Grant, F.J., Heipel, M.D., Burkhead, S.K., and Kramer, J.M. (1994). Cloning and expression of murine thrombopoietin cDNA and stimulation of platelet production in vivo. Nature *369*, 565–568. https://doi.org/10.1038/369565a0.

4. Bartley, T.D., Bogenberger, J., Hunt, P., Li, Y.S., Lu, H.S., Martin, F., Chang, M.S., Samal, B., Nichol, J.L., and Swift, S. (1994). Identification and cloning of a megakaryocyte growth and development factor that is a ligand for the cytokine receptor Mpl. Cell *77*, 1117–1124. https://doi.org/10.1016/0092-8674(94)90450-2.

5. De Sauvage, F.J., Hass, P.E., Spencer, S.D., Malloy, B.E., Gurney, A.L., Spencer, S.A., Darbonne, W.C., Henzel, W.J., Wong, S.C., and Kuang, W.J. (1994). Stimulation of megakaryocytopoiesis and thrombopoiesis by the c-Mpl ligand. Nature *369*, 533–538. https://doi.org/10.1038/369533a0.

6. Cornish, N., Aungraheeta, M.R., FitzGibbon, L., Burley, K., Alibhai, D., Collins, J., Greene, D., Downes, K., NIHR BioResource, and Westbury, S.K., et al. (2020). Monoallelic loss-of-function THPO variants cause heritable thrombocytopenia. Blood Adv. *4*, 920–924. https://doi.org/10.1182/bloodadvances.2019001293.

7. Noris, P., Marconi, C., De Rocco, D., Melazzini, F., Pippucci, T., Loffredo, G., Giangregorio, T., Pecci, A., Seri, M., and Savoia, A. (2018). A new form of inherited thrombocytopenia due to monoallelic loss of function mutation in the thrombopoietin gene. Br. J. Haematol. *181*, 698–701. https://doi.org/10.1111/bjh.14694.

8. Pecci, A., Ragab, I., Bozzi, V., De Rocco, D., Barozzi, S., Giangregorio, T., Ali, H., Melazzini, F., Sallam, M., Alfano, C., et al. (2018). Thrombopoietin mutation in congenital amegakaryocytic thrombocytopenia treatable with Romiplostim. EMBO Mol. Med. *10*, 63–75. https://doi.org/10.15252/emmm.201708168.

9. Pikman, Y., Lee, B.H., Mercher, T., McDowell, E., Ebert, B.L., Gozo, M., Cuker, A., Wernig, G., Moore, S., Galinsky, I., et al. (2006). MPLW515L is a novel somatic activating mutation in myelofibrosis with myeloid metaplasia. PLoS Med. *3*, e270. https://doi.org/10.1371/journal.pmed.0030270.

10. Ding, J., Komatsu, H., Wakita, A., Kato-Uranishi, M., Ito, M., Satoh, A., Tsuboi, K., Nitta, M., Miyazaki, H., Iida, S., et al. (2004). Familial essential thrombocythemia associated with a dominant-positive activating mutation of the c-MPL gene, which encodes for the receptor for thrombopoietin. Blood *103*, 4198–4200. https://doi.org/10.1182/blood-2003-10-3471.

11. Beer, P.A., Campbell, P.J., Scott, L.M., Bench, A.J., Erber, W.N., Bareford, D., Wilkins, B.S., Reilly, J.T., Hasselbalch, H.C., Bowman, R., et al. (2008). MPL mutations in myeloproliferative disorders: analysis of the PT-1 cohort. Blood *112*, 141–149. https://doi.org/10.1182/blood-2008-01-131664.

12. Baxter, E.J., Scott, L.M., Campbell, P.J., East, C., Fourouclas, N., Swanton, S., Vassiliou, G.S., Bench, A.J., Boyd, E.M., Curtin, N., et al. (2005). Acquired mutation of the tyrosine kinase JAK2 in human myeloproliferative disorders. Lancet *365*, 1054–1061. https://doi.org/10.1016/S0140-6736(05)71142-9.

13. Levine, R.L., Wadleigh, M., Cools, J., Ebert, B.L., Wernig, G., Huntly, B.J.P., Boggon, T.J., Wlodarska, I., Clark, J.J., Moore, S., et al. (2005). Activating mutation in the tyrosine kinase JAK2 in polycythemia vera,

essential thrombocythemia, and myeloid metaplasia with myelofibrosis. Cancer Cell *7*, 387–397. https://doi.org/10.1016/j.ccr.2005.03.023.

14. Klampfl, T., Gisslinger, H., Harutyunyan, A.S., Nivarthi, H., Rumi, E., Milosevic, J.D., Them, N.C.C., Berg, T., Gisslinger, B., Pietra, D., et al. (2013). Somatic mutations of calreticulin in myeloproliferative neoplasms. N. Engl. J. Med. *369*, 2379–2390. https://doi.org/10.1056/NEJMoa1311347.
15. Nangalia, J., Massie, C.E., Baxter, E.J., Nice, F.L., Gundem, G., Wedge, D.C., Avezov, E., Li, J., Kollmann, K., Kent, D.G., et al. (2013). Somatic *CALR* mutations in myeloproliferative neoplasms with nonmutated *JAK2*. N. Engl. J. Med. *369*, 2391–2405. https://doi.org/10.1056/NEJMoa1312542.
16. Stasi, R. (2009). Eltrombopag: the discovery of a second generation thrombopoietin-receptor agonist. Expert Opin. Drug Discov. *4*, 85–93. https://doi.org/10.1517/17460440802642484.
17. Cines, D.B., Yasothan, U., and Kirkpatrick, P. (2008). Romiplostim. Nat. Rev. Drug Discov. *7*, 887–888. https://doi.org/10.1038/nrd2741.
18. Kuter, D.J. (2022). The structure, function, and clinical use of the thrombopoietin receptor agonist avatrombopag. Blood Rev. *53*, 100909. https://doi.org/10.1016/j.blre.2021.100909.
19. Deng, J., Hu, H., Huang, F., Huang, C., Huang, Q., Wang, L., Wu, A., Yang, J., Qin, D., Zou, W., et al. (2021). Comparative efficacy and safety of thrombopoietin receptor agonists in adults with thrombocytopenia: a systematic review and network meta-analysis of randomized controlled trial. Front. Pharmacol. *12*, 704093. https://doi.org/10.3389/fphar.2021.704093.
20. Ghanima, W., Cooper, N., Rodeghiero, F., Godeau, B., and Bussel, J.B. (2019). Thrombopoietin receptor agonists: ten years later. Haematologica *104*, 1112–1123. https://doi.org/10.3324/haematol.2018.212845.
21. Ghanima, W., Geyer, J.T., Lee, C.S., Boiocchi, L., Imahiyerobo, A.A., Orazi, A., and Bussel, J.B. (2014). Bone marrow fibrosis in 66 patients with immune thrombocytopenia treated with thrombopoietin-receptor agonists: a single-center, long-term follow-up. Haematologica *99*, 937–944. https://doi.org/10.3324/haematol.2013.098921.
22. Miller, C.L., and Eaves, C.J. (1997). Expansion in vitro of adult murine hematopoietic stem cells with transplantable lympho-myeloid reconstituting ability. Proc. Natl. Acad. Sci. USA *94*, 13648–13653. https://doi.org/10.1073/pnas.94.25.13648.
23. Zhang, C.C., and Lodish, H.F. (2008). Cytokines regulating hematopoietic stem cell function. Curr. Opin. Hematol. *15*, 307–311. https://doi.org/10.1097/MOH.0b013e3283007db5.
24. Li, J., Wang, X., Ding, J., Zhu, Y., Min, W., Kuang, W., Yuan, K., Sun, C., and Yang, P. (2022). Development and clinical advancement of small molecules for ex vivo expansion of hematopoietic stem cell. Acta Pharm. Sin. B *12*, 2808–2831. https://doi.org/10.1016/j.apsb.2021.12.006.
25. Wilkinson, A.C., Ishida, R., Kikuchi, M., Sudo, K., Morita, M., Crisostomo, R.V., Yamamoto, R., Loh, K.M., Nakamura, Y., Watanabe, M., et al. (2019). Long-term ex vivo haematopoietic-stem-cell expansion allows nonconditioned transplantation. Nature *571*, 117–121. https://doi.org/10.1038/s41586-019-1244-x.
26. Bernitz, J.M., Kim, H.S., MacArthur, B., Sieburg, H., and Moore, K. (2016). Hematopoietic stem cells count and remember self-renewal divisions. Cell *167*, 1296–1309.e10. https://doi.org/10.1016/j.cell.2016.10.022.
27. Wilmes, S., Hafer, M., Vuorio, J., Tucker, J.A., Winkelmann, H., Löchte, S., Stanly, T.A., Pulgar Prieto, K.D., Poojari, C., Sharma, V., et al. (2020). Mechanism of homodimeric cytokine receptor activation and dysregulation by oncogenic mutations. Science *367*, 643–652. https://doi.org/10.1126/science.aaw3242.
28. Pecquet, C., Chachoua, I., Roy, A., Balligand, T., Vertenoeil, G., Leroy, E., Albu, R.I., Defour, J.P., Nivarthi, H., Hug, E., et al. (2019). Calreticulin mutants as oncogenic rogue chaperones for TpoR and traffic-defective pathogenic TpoR mutants. Blood *133*, 2669–2681. https://doi.org/10.1182/blood-2018-09-874578.
29. Di Buduo, C.A., Currao, M., Pecci, A., Kaplan, D.L., Balduini, C.L., and Balduini, A. (2016). Revealing eltrombopag's promotion of human megakaryopoiesis through AKT/ERK-dependent pathway activation. Haematologica *101*, 1479–1488. https://doi.org/10.3324/haematol.2016.146746.
30. Cui, L., Moraga, I., Lerbs, T., Van Neste, C., Wilmes, S., Tsutsumi, N., Trotman-Grant, A.C., Gakovic, M., Andrews, S., Gotlib, J., et al. (2021). Tuning MPL signaling to influence hematopoietic stem cell differentiation and inhibit essential thrombocythemia progenitors. Proc. Natl. Acad. Sci. USA *118*, e2017849118. https://doi.org/10.1073/pnas.2017849118.
31. Saxton, R.A., Glassman, C.R., and Garcia, K.C. (2022). Emerging principles of cytokine pharmacology and therapeutics. Nat. Rev. Drug Discov. *22*, 21–37. https://doi.org/10.1038/s41573-022-00557-6.
32. Villanueva, M.T. (2022). Virtual screening yields refined GPCR agonists. Nat. Rev. Drug Discov. *21*, 879. https://doi.org/10.1038/d41573-022-00177-0.
33. Hitchcock, I.S., Hafer, M., Sangkhae, V., and Tucker, J.A. (2021). The thrombopoietin receptor: revisiting the master regulator of platelet production. Platelets *32*, 770–778. https://doi.org/10.1080/09537104.2021.1925102.
34. Sasazawa, Y., Sato, N., Suzuki, T., Dohmae, N., and Simizu, S. (2015). C-mannosylation of thrombopoietin receptor (c-Mpl) regulates thrombopoietin-dependent JAK-STAT signaling. Biochem. Biophys. Res. Commun. *468*, 262–268. https://doi.org/10.1016/j.bbrc.2015.10.116.
35. Ocampo Daza, D., and Larhammar, D. (2018). Evolution of the receptors for growth hormone, prolactin, erythropoietin and thrombopoietin in relation to the vertebrate tetraploidizations. Gen. Comp. Endocrinol. *257*, 143–160. https://doi.org/10.1016/j.ygcen.2017.06.021.
36. Livnah, O., Stura, E.A., Johnson, D.L., Middleton, S.A., Mulcahy, L.S., Wrighton, N.C., Dower, W.J., Jolliffe, L.K., and Wilson, I.A. (1996). Functional mimicry of a protein hormone by a peptide agonist: the EPO receptor complex at 2.8 Å. Science *273*, 464–471. https://doi.org/10.1126/science.273.5274.464.
37. Syed, R.S., Reid, S.W., Li, C., Cheetham, J.C., Aoki, K.H., Liu, B., Zhan, H., Osslund, T.D., Chirino, A.J., Zhang, J., et al. (1998). Efficiency of signalling through cytokine receptors depends critically on receptor orientation. Nature *395*, 511–516. https://doi.org/10.1038/26773.
38. de Vos, A.M., Ultsch, M., and Kossiakoff, A.A. (1992). Human growth hormone and extracellular domain of its receptor: crystal structure of the complex. Science *255*, 306–312. https://doi.org/10.1126/science.1549776.
39. van Agthoven, J., Zhang, C., Tallet, E., Raynal, B., Hoos, S., Baron, B., England, P., Goffin, V., and Broutin, I. (2010). Structural characterization of the stem-stem dimerization interface between prolactin receptor chains complexed with the natural hormone. J. Mol. Biol. *404*, 112–126. https://doi.org/10.1016/j.jmb.2010.09.036.
40. Staerk, J., Defour, J.P., Pecquet, C., Leroy, E., Antoine-Poirel, H., Brett, I., Itaya, M., Smith, S.O., Vainchenker, W., and Constantinescu, S.N. (2011). Orientation-specific signalling by thrombopoietin receptor dimers. EMBO J. *30*, 4398–4413. https://doi.org/10.1038/emboj.2011.315.
41. Glassman, C.R., Tsutsumi, N., Saxton, R.A., Lupardus, P.J., Jude, K.M., and Garcia, K.C. (2022). Structure of a Janus kinase cytokine receptor complex reveals the basis for dimeric activation. Science *376*, 163–169. https://doi.org/10.1126/science.abn8933.
42. Caveney, N.A., Saxton, R.A., Waghray, D., Glassman, C.R., Tsutsumi, N., Hubbard, S.R., and Garcia, K.C. (2023). Structural basis of Janus kinase trans-activation. Cell Rep. *42*, 112201. https://doi.org/10.1016/j.celrep.2023.112201.
43. Vondrášek, J., Mason, P.E., Heyda, J., Collins, K.D., and Jungwirth, P. (2009). The molecular origin of like-charge arginine-arginine pairing in water. J. Phys. Chem. B *113*, 9041–9045. https://doi.org/10.1021/jp902377q.
44. Mendoza, J.L., Escalante, N.K., Jude, K.M., Sotolongo Bellon, J., Su, L., Horton, T.M., Tsutsumi, N., Berardinelli, S.J., Haltiwanger, R.S., Piehler, J., et al. (2019). Structure of the IFNγ receptor complex guides design of biased agonists. Nature *567*, 56–60. https://doi.org/10.1038/s41586-019-0988-7.

45. Mohan, K., Ueda, G., Kim, A.R., Jude, K.M., Fallas, J.A., Guo, Y., Hafer, M., Miao, Y., Saxton, R.A., Piehler, J., et al. (2019). Topological control of cytokine receptor signaling induces differential effects in hematopoiesis. Science *364*. https://doi.org/10.1126/science.aav7532.

46. Zimran, E., Papa, L., and Hoffman, R. (2021). Ex vivo expansion of hematopoietic stem cells: finally transitioning from the lab to the clinic. Blood Rev. *50*, 100853. https://doi.org/10.1016/j.blre.2021.100853.

47. Sakurai, M., Ishitsuka, K., Ito, R., Wilkinson, A.C., Kimura, T., Mizutani, E., Nishikii, H., Sudo, K., Becker, H.J., Takemoto, H., et al. (2023). Chemically defined cytokine-free expansion of human haematopoietic stem cells. Nature *615*, 127–133. https://doi.org/10.1038/s41586-023-05739-9.

48. Grey, W., Chauhan, R., Piganeau, M., Huerga Encabo, H.H., Garcia-Albornoz, M., McDonald, N.Q., and Bonnet, D. (2020). Activation of the receptor tyrosine kinase RET improves long-term hematopoietic stem cell outgrowth and potency. Blood *136*, 2535–2547. https://doi.org/10.1182/BLOOD.2020006302.

49. Lehnertz, B., Chagraoui, J., MacRae, T., Tomellini, E., Corneau, S., Mayotte, N., Boivin, I., Durand, A., Gracias, D., and Sauvageau, G. (2021). HLF expression defines the human hematopoietic stem cell state. Blood *138*, 2642–2654. https://doi.org/10.1182/blood.2021010745.

50. Yoshihara, H., Arai, F., Hosokawa, K., Hagiwara, T., Takubo, K., Nakamura, Y., Gomei, Y., Iwasaki, H., Matsuoka, S., Miyamoto, K., et al. (2007). Thrombopoietin/MPL signaling regulates hematopoietic stem cell quiescence and interaction with the osteoblastic niche. Cell Stem Cell *1*, 685–697. https://doi.org/10.1016/j.stem.2007.10.020.

51. Nakamura-Ishizu, A., and Suda, T. (2020). Multifaceted roles of thrombopoietin in hematopoietic stem cell regulation. Ann. N. Y. Acad. Sci. *1466*, 51–58. https://doi.org/10.1111/nyas.14169.

52. Qian, H., Buza-Vidas, N., Hyland, C.D., Jensen, C.T., Antonchuk, J., Månsson, R., Thoren, L.A., Ekblom, M., Alexander, W.S., and Jacobsen, S.E.W. (2007). Critical role of thrombopoietin in maintaining adult quiescent hematopoietic stem cells. Cell Stem Cell *1*, 671–684. https://doi.org/10.1016/j.stem.2007.10.008.

53. Boiocchi, L., Orazi, A., Ghanima, W., Arabadjief, M., Bussel, J.B., and Geyer, J.T. (2012). Thrombopoietin receptor agonist therapy in primary immune thrombocytopenia is associated with bone marrow hypercellularity and mild reticulin fibrosis but not other stromal abnormalities. Mod. Pathol. *25*, 65–74. https://doi.org/10.1038/modpathol.2011.128.

54. Wilkinson, A.C., Igarashi, K.J., and Nakauchi, H. (2020). Haematopoietic stem cell self-renewal in vivo and ex vivo. Nat. Rev. Genet. *21*, 541–554. https://doi.org/10.1038/s41576-020-0241-0.

55. Naldini, L., Cicalese, M.P., Bernardo, M.E., Gentner, B., Gabaldo, M., Ferrari, G., and Aiuti, A. (2022). The EHA research roadmap: hematopoietic stem cell gene therapy. Hemasphere *6*, e671. https://doi.org/10.1097/HS9.0000000000000671.

56. Chabannon, C., Kuball, J., Bondanza, A., Dazzi, F., Pedrazzoli, P., Toubert, A., Ruggeri, A., Fleischhauer, K., and Bonini, C. (2018). Hematopoietic stem cell transplantation in its 60s: A platform for cellular therapies. Sci. Transl. Med. *10*, 1–11. https://doi.org/10.1126/scitranslmed.aap9630.

57. Fares, I., Chagraoui, J., Gareau, Y., Gingras, S., Ruel, R., Mayotte, N., Csaszar, E., Knapp, D.J.H.F., Miller, P., Ngom, M., et al. (2014). Cord blood expansion. Pyrimidoindole derivatives are agonists of human hematopoietic stem cell self-renewal. Science *345*, 1509–1512. https://doi.org/10.1126/science.1256337.

58. Ciusss de L'Est de l'Île de Montréal (2000). UM171 expanded cord blood in patients with high-risk acute leukemia/myelodysplasia. NLM Identifier NCT03913026 (National Library of Medicine). https://clinicaltrials.gov/show/NCT03913026.

59. Bellón, J.S., Birkholz, O., Richter, C.P., Eull, F., Kenneweg, H., Wilmes, S., Rothbauer, U., You, C., Walter, M.R., Kurre, R., et al. (2022). Four-color single-molecule imaging with engineered tags resolves the molecular architecture of signaling complexes in the plasma membrane. Cell Rep Methods *4*, 100165. https://doi.org/10.1016/j.crmeth.2022.100165.

60. Götzke, H., Kilisch, M., Martínez-Carranza, M., Sograte-Idrissi, S., Rajavel, A., Schlichthaerle, T., Engels, N., Jungmann, R., Stenmark, P., Opazo, F., et al. (2019). The ALFA-tag is a highly versatile tool for nanobody-based bioscience applications. Nat. Commun. *10*, 4403. https://doi.org/10.1038/s41467-019-12301-7.

61. Reeves, P.J., Callewaert, N., Contreras, R., and Khorana, H.G. (2002). Structure and function in rhodopsin: high-level expression of rhodopsin with restricted and homogeneous N-glycosylation by a tetracycline-inducible N-acetylglucosaminyltransferase I-negative HEK293S stable mammalian cell line. Proc. Natl. Acad. Sci. U S A *99*, 13419–13424. https://doi.org/10.1073/pnas.212519299.

62. Zheng, S.Q., Palovcak, E., Armache, J.P., Verba, K.A., Cheng, Y., and Agard, D.A. (2017). MotionCor2: anisotropic correction of beam-induced motion for improved cryo-electron microscopy. Nat. Methods *14*, 331–332. https://doi.org/10.1038/nmeth.4193.

63. Mastronarde, D.N. (2005). Automated electron microscope tomography using robust prediction of specimen movements. J Sruct Biol *152*, 36–51. https://doi.org/10.1016/j.jsb.2005.07.007.

64. Punjani, A., Rubinstein, J.L., Fleet, D.J., and Brubaker, M.A. (2017). CryoSPARC: algorithms for rapid unsupervised cryo-EM structure determination. Nat. Methods *14*, 290–296. https://doi.org/10.1038/nmeth.4169.

65. Emsley, P., and Cowtan, K. (2004). Coot: model-building tools for molecular graphics. Acta Crystallogr D Biol Crystallogr *60*, 2126–2132. https://doi.org/10.1107/S0907444904019158.

66. Liebschner, D., Afonine, P.V., Baker, M.L., Bunkóczi, G., Chen, V.B., Croll, T.I., Hintze, B., Hung, L.W., Jain, S., McCoy, A.J., et al. (2019). Macromolecular structure determination using X-rays, neutrons and electrons: recent developments in Phenix. Acta Crystallogr. D Struct. Biol. *75*, 861–877. https://doi.org/10.1107/S2059798319011471.

67. Croll, T.I. (2018). ISOLDE: a physically realistic environment for model building into low-resolution electron-density maps. Acta Crystallogr. D Struct. Biol. *74*, 519–530. https://doi.org/10.1107/S2059798318002425.

68. Pettersen, E.F., Goddard, T.D., Huang, C.C., Couch, G.S., Greenblatt, D.M., Meng, E.C., and Ferrin, T.E. (2004). UCSF Chimera–a visualization system for exploratory research and analysis. J. Comput. Chem. *25*, 1605–1612. https://doi.org/10.1002/jcc.20084.

69. Pettersen, E.F., Goddard, T.D., Huang, C.C., Meng, E.C., Couch, G.S., Croll, T.I., Morris, J.H., and Ferrin, T.E. (2021). UCSF ChimeraX: Structure visualization for researchers, educators, and developers. Protein Sci *30*, 70–82. https://doi.org/10.1002/pro.3943.

70. Morin, A., Eisenbraun, B., Key, J., Sanschagrin, P.C., Timony, M.A., Ottaviano, M., and Sliz, P. (2013). Collaboration gets the most out of software. Elife *2*, e01456. https://doi.org/10.7554/eLife.01456.

71. Lawrence, M.C., and Colman, P.M. (1993). Shape complementarity at protein/protein interfaces. J. Mol. Biol. *234*, 946–950. https://doi.org/10.1006/jmbi.1993.1648.

72. Dukkipati, A., Park, H.H., Waghray, D., Fischer, S., and Garcia, K.C. (2008). BacMam system for high-level expression of recombinant soluble and membrane glycoproteins for structural studies. Protein Expr. Purif. *62*, 160–170. https://doi.org/10.1016/j.pep.2008.08.004.

73. Sanchez-Garcia, R., Gomez-Blanco, J., Cuervo, A., Carazo, J., Sorzano, C., and Vargas, J. (2020). DeepEMhancer: a deep learning solution for cryo-EM volume post-processing. Commun. Biol. *4*, 874. https://doi.org/10.1101/2020.06.12.148296.

74. Joosten, R.P., te Beek, T.A., Krieger, E., Hekkelman, M.L., Hooft, R.W., Schneider, R., Sander, C., and Vriend, G. (2011). A series of PDB related databases for everyday needs. Nucleic Acids Res. *39*, D411–D419. https://doi.org/10.1093/nar/gkq1105.

75. Wojtowicz, W.M., Vielmetter, J., Fernandes, R.A., Siepe, D.H., Eastman, C.L., Chisholm, G.B., Cox, S., Klock, H., Anderson, P.W., Rue, S.M., et al. (2020). A human IgSF cell-surface interactome reveals a complex network of protein-protein interactions. Cell *182*, 1027–1043.e17. https://doi.org/10.1016/j.cell.2020.07.025.

76. Rix, B., Maduro, A.H., Bridge, K.S., and Grey, W. (2022). Markers for human haematopoietic stem cells: the disconnect between an identification marker and its function. Front. Physiol. *13*, 1009160. https://doi.org/10.3389/fphys.2022.1009160.

77. Fares, I., Chagraoui, J., Lehnertz, B., MacRae, T., Mayotte, N., Tomellini, E., Aubert, L., Roux, P.P., and Sauvageau, G. (2017). EPCR expression marks UM171-expanded CD34+ cord blood stem cells. Blood *129*, 3344–3351. https://doi.org/10.1182/blood-2016-11-750729.

78. Graham, F.L., and van der Eb, A.J. (1973). A new technique for the assay of infectivity of human adenovirus 5 DNA. Virology *52*, 456–467. https://doi.org/10.1016/0042-6822(73)90341-3.

79. You, C., Richter, C.P., Löchte, S., Wilmes, S., and Piehler, J. (2014). Dynamic submicroscopic signaling zones revealed by pair correlation tracking and localization microscopy. Anal. Chem. *86*, 8593–8602. https://doi.org/10.1021/ac501127r.

80. Vogelsang, J., Kasper, R., Steinhauer, C., Person, B., Heilemann, M., Sauer, M., and Tinnefeld, P. (2008). A reducing and oxidizing system minimizes photobleaching and blinking of fluorescent dyes. Angew. Chem. Int. Ed. Engl. *47*, 5465–5469. https://doi.org/10.1002/anie.200801518.

81. Edelstein, A.D., Tsuchida, M.A., Amodaj, N., Pinkard, H., Vale, R.D., and Stuurman, N. (2014). Advanced methods of microscope control using μManager software. J. Biol. Methods *1*, 1–18. https://doi.org/10.14440/jbm.2014.36.

82. Sergé, A., Bertaux, N., Rigneault, H., and Marguet, D. (2008). Dynamic multiple-target tracing to probe spatiotemporal cartography of cell membranes. Nat. Methods *5*, 687–694. https://doi.org/10.1038/nmeth.1233.

Please cite this article in press as: Tsutsumi et al., Structure of the thrombopoietin-MPL receptor complex is a blueprint for biasing hematopoiesis, Cell (2023), https://doi.org/10.1016/j.cell.2023.07.037

STAR★METHODS

KEY RESOURCES TABLE

REAGENT or RESOURCE	SOURCE	IDENTIFIER
Antibodies		
Rat anti-mouse Sca1, clone D7, Brilliant Violet 605 conjugated (dilution 1:100)	Biolegend	Cat# 108133; RRID:AB_2562275
Rat anti-mouse CD16/32, clone 93, Brilliant Violet BV711 conjugated (dilution 1:500)	Biolegend	Cat# 101337; RRID:AB_2565637
Rat anti-mouse CD34, clone RAM34, FITC conjugated (dilution 1:100)	BD Pharmingen	Cat# 560238; RRID:AB_1645242
Armenian Hamster anti-mouse CD3e, clone: 145-2C11, PE/Cy7 conjugated (dilution 1:1000)	Biolegend	Cat# 100320; RRID:AB_312685
Rat anti-mouse/ human CD11b, clone: M1/70, PE/Cy7 conjugated (dilution 1:1000)	Biolegend	Cat# 101216; RRID:AB_312799
Rat anti-mouse Ter119/ erythroid cells, clone: Ter119, PE/Cy7 conjugated (dilution 1:1000)	Biolegend	Cat #116221; RRID:AB_2137789
Rat anti-mouse CD19, clone: eBio 1D3, PE/Cy7 conjugated (dilution 1:1000)	eBioscience	Cat# 25-0193-82; RRID:AB_657663
Rat anti-mouse Gr1, clone: RB6-8C5, PE/Cy7 conjugated (dilution 1:1000)	Biolegend	Cat# 108416; RRID:AB_313381
Rat anti-mouse CD135, clone: A2F10, PE/Cy5 conjugated (dilution 1:500)	Biolegend	Cat# 135312; RRID:AB_2263031
Rat anti-mouse CD117 (c-Kit), clone: 2B8, APC/Cy7 conjugated (dilution 1:100)	Biolegend	Cat# 105825; RRID:AB_1626280
Rat anti-mouse CD201 (EPCR), clone: 1560, PE conjugated (dilution 1:100)	STEMCELL Technologies	Cat# 60038PE
Rat anti-mouse CD41, clone: MWReg30, PE conjugated (dilution 1:100)	Biolegend	Cat# 133906; RRID:AB_2129745
Rat anti-mouse CD41, clone: MWReg30, FITC conjugated (dilution 1:200)	Invitrogen	Cat# 13-0411-82; RRID:AB_763484
Mouse anti-human CD34, clone: 581, APC conjugated (dilution 1:100)	BD Pharmingen	Cat# 555824; RRID:AB_398614
Mouse anti-human CD34, clone: 581, PE/Cy7 conjugated (dilution 1:100)	BD Pharmingen	Cat# 560710; RRID:AB_1727470
Mouse anti-human CD45RA, clone: HI100, APC-eFluor conjugated (dilution 1:100)	eBioscience	Cat# 47-0458-42; RRID:AB_10853641
Mouse anti-human CD45RA, clone: HI100, PE/Cy7 conjugated (dilution 1:100)	eBioscience	Cat# 25-0458-42; RRID:AB_1548774
Mouse anti-human CD90, clone: 5E10, PE conjugated (dilution 1:100)	BD Pharmingen	Cat# 561970; RRID:AB_10894194
Rat anti-human CD201 (EPCR), clone: RCR-252, BV421 conjugated (dilution 1:100)	BD OptiBuild	Cat# 743552; RRID:AB_2741576
Rat anti-human CD201 (EPCR), clone: RCR-252, PE conjugated (dilution 1:100)	BD Pharmingen	Cat# 557950; RRID:AB_647192
Mouse anti-mouse/ human pSTAT1 (Ser272), clone: A15158B, Alexa Fluor 488 conjugated (dilution 1:100)	Biolegend	Cat# 686409; RRID:AB_2650783
Mouse anti-human pSTAT1 (Tyr701), clone: A17012A, Alexa Fluor 647 conjugated (dilution 1:100)	Biolegend	Cat# 666409; RRID:AB_2814502

(*Continued on next page*)

Please cite this article in press as: Tsutsumi et al., Structure of the thrombopoietin-MPL receptor complex is a blueprint for biasing hematopoiesis, Cell (2023), https://doi.org/10.1016/j.cell.2023.07.037

Continued

REAGENT or RESOURCE	SOURCE	IDENTIFIER
Mouse anti-human pSTAT3 (Ser727), clone: A16089B, Alexa Fluor 647 conjugated (dilution 1:100)	Biolegend	Cat# 698913; RRID:AB_2750259
Mouse anti-mouse/ human pSTAT3 (Tyr705), clone: 13A3-1, Alexa Fluor 488 conjugated (dilution 1:100)	Biolegend	Cat# 651005; RRID:AB_2572083
Mouse anti-human pSTAT5 (Tyr694), clone: 47, Alexa Fluor 647 conjugated (dilution 1:100)	BD Phosflow	Cat# 612599; RRID:AB_399882
Rabbit anti-human pJAK2 (Tyr1007/ Tyr1008), clone: E132, Alexa Fluor 488 conjugated (dilution 1:100)	Abcam	Cat# ab200339
Mouse anti-human pERK1/2 (Thr202/ Tyr204), clone: 20A, Alexa Fluor 488 conjugated (dilution 1:100)	BD Phosflow	Cat# 612592; RRID:AB_399875
Mouse anti-human pAKT (Ser473), clone: M89-61, Alexa Fluor 647 conjugated (dilution 1:100)	BD Phosflow	Cat# 560343; RRID:AB_1645397
Rabbit anti-human pAKT (Thr308), clone: D25E6, Alexa Fluor 647 conjugated (dilution 1:100)	Cell Signalling Technology	Cat# 48646S
Rabbit anti-human pCREB (Ser133), clone: 87G3, Alexa Fluor 488 conjugated (dilution 1:100)	Cell Signalling Technology	Cat# 9187S
Mouse anti-human pMEK1 (Ser298), clone: A16117B, APC conjugated (dilution 1:100)	Biolegend	Cat# 610607; RRID:AB_2888737
Mouse anti-human pmTOR (Ser2448), clone: O21-404, PE conjugated (dilution 1:100)	BD Phosflow	Cat# 563489; RRID:AB_2736872
Rabbit anti-human mTOR, clone: 7C10, Alexa Fluor 647 conjugated (dilution 1:100)	Cell Signalling Technology	Cat# 5048S
Rabbit anti-human IRF-1, clone: D5E4, Alexa Fluor 647 conjugated (dilution 1:100)	Cell Signalling Technology	Cat# 14105S
Rat IgG1, κ Isotype control, clone: RTK2071, Biotin (dilution 1:200)	Biolegend	Cat# 400403; RRID:AB_326509
Rat anti-mouse CD41a, clone: MWReg30, Biotin (dilution 1:200)	Invitrogen	Cat# 13-0411-85; RRID:AB_763489
Biological samples		
Homo sapiens: $CD34^+$ cells	Anthony Nolan Trust	N/A
Chemicals, peptides, and recombinant proteins		
Lauryl Maltose Neopentyl Glycol (LMNG)	Anatrace	Cat# NG310
Digitonin	Millipore	Cat# 300410
Protease Inhibitor Cocktail	Sigma-Aldrich	Cat# P8849
cOmplete Protease Inhibitor Cocktail	Roche	Cat# 05056489001
BS3 (bis(sulfosuccinimidyl)suberate)	Thermo Scientific	Cat# A39266
HEPES	Fisher Scientific	Cat# BP310
Sodium Hydroxide Solution (10N/Certified)	Fisher Scientific	Cat# SS255-1
Tris Base	Fisher Scientific	Cat# BP152
Tris Hydrochloride	Fisher Scientific	Cat# BP153
Glycerol	Fisher Scientific	Cat# BP229
Sodium Chloride	Fisher Scientific	Cat# S271
Calcium chloride dihydrate	Sigma-Aldrich	Cat# C7902

(*Continued on next page*)

Please cite this article in press as: Tsutsumi et al., Structure of the thrombopoietin-MPL receptor complex is a blueprint for biasing hematopoiesis, Cell (2023), https://doi.org/10.1016/j.cell.2023.07.037

Continued

REAGENT or RESOURCE	SOURCE	IDENTIFIER
TCEP solution	Thermo Scientific	Cat# 77720
EDTA	Fisher Scientific	Cat# BP120
FLAG peptide	GenScript	N/A
Imidazole	ACROS Organics	Cat# 122025000
FreeStyle 293 Expression Medium	Thermo Fisher	Cat# 12338026
ExpiFectamine 293 Transfection Kit	Thermo Fisher Scientific	Cat# A14525
Expi293 Expression Medium	Thermo Fisher Scientific	Cat# A1435101
Sf-900 III SFM (Serum-Free Media)	Thermo Fisher	Cat# 12658019
GlutaMAX	Thermo Fisher	Cat# 35050079
Fetal Bovine Serum (FBS) (for Sf9 cells)	Sigma-Aldrich	Cat# F7524
Sodium butyrate	Sigma-Aldrich	Cat# 303410
FuGENE HD Transfection Reagent	Promega	Cat# E2312
Lipofectamine 2000 transfection reagent	Invitrogen	Cat# 11668019
Biotinylated ectodomain of MPL	Cancer Research Horizons	N/A
HBS-EP+ Buffer 10×	Cytiva	Cat# BR100826
PBS, pH 7.2	Gibco	Cat# 20012027
Dulbecco's Modified Eagle's Medium (DMEM)	Gibco	Cat# 21969-035
L-glutamine	Gibco	Cat# 25030-024
FBS (for HEK293T, UT7/TPO and $CD34^+$ cells)	Gibco	Cat# A5256701
Penicillin/Streptomycin	Gibco	Cat# 15140-122
jetPRIME transfection reagent and buffer	Polyplus Transfections	Cat# 101000001
Roswell Park Memorial Institute (RPMI) 1640 medium	Gibco	Cat# 31870-025
recombinant human TPO (rhTPO)	Zymogenetics	N/A
CyQUANT (2,3-bis-(2-methoxy-4-nitro-5-sulfophenyl)-2H-tetrazolium-5-carboxanilide) (XTT) reagent	Invitrogen	Cat# X12223
paraformaldehyde (PFA)	Thermo Fisher Scientific	Cat# 28906
bovine serum albumin (BSA)	Fisher Scientific	Cat# BP1660-100
sodium azide	Severn Biotech	Cat# 40-2010-101
DyLight800 NHS Ester	Thermo Scientific	Cat# 46422
Pacific Blue Succinimidyl Ester	Stratech	Cat# 570-AAT
Dimethyl sulfoxide (DMSO)	Sigma-Aldrich	D2650-5X5ml
human TruStain FX	Biolegend	Cat# 422302
Pierce High Capacity Endotoxin Removal Spin Columns	Thermo Fisher	Cat# 88274
Zombie Aqua	Biolegend	Cat# 423107
Stem cell factor (SCF)	Biolegend	Cat# 573906
Flt3L	Biolegend	Cat# 550606
hTPO	Peprotech	Cat# 300-18
sucrose	Fisher Scientific	Cat# S/8600/60
acetone	Fisher Scientific	Cat# A/0600/PB17
ReadyProbes Avidin/Biotin Blocking Solution	Invitrogen	Cat# R37627
DAPI	Biolegend	Cat# 422801
Prolong Gold	Invitrogen	Cat# P36934
StemSpan SFEM II	STEMCELL Technologies	Cat# 09605
Precision Count Beads	Biolegend	Cat# 424902

(*Continued on next page*)

Please cite this article in press as: Tsutsumi et al., Structure of the thrombopoietin-MPL receptor complex is a blueprint for biasing hematopoiesis, Cell (2023), https://doi.org/10.1016/j.cell.2023.07.037

Continued

REAGENT or RESOURCE	SOURCE	IDENTIFIER
methanol	Fisher Scientific	Cat# M/4056/PB17
Streptavidin, Alexa Fluor™ 546 conjugate	Invitrogen	Cat# S11225
Rat serum	Merck	Cat# R9759
MEM Eagle medium	PAN Biotech	Cat# P04-09500
Stable Glutamine	PAN Biotech	Cat# K0302
Phenol red-free MEM	PAN Biotech	Cat# P04-02500S1
FBS superior (for HeLa cells)	Merck	Cat# S0615
PBS (for HeLa cells)	PAN Biotech	Cat# P04-36500
MEM NEAA	PAN Biotech	Cat# P08-32100
Glucose	Carl Roth	Cat# 3774.1
Glucose Oxidase	Sigma-Aldrich	Cat# 9001-37-0
Catalase	Sigma-Aldrich	Cat# C-40
Methylviologen	Sigma-Aldrich	Cat# 856177
Ascorbic acid	Sigma-Aldrich	Cat# A-4544
Poly-L-lysine (PLL)-poly(ethylene) glycol (PEG)-RGD	Bellón et al.[59]	N/A
TetraSpeck beads 0.1 μm	Thermo Fisher	Cat# T7279
Maleimide ATTO 643	Atto-tec	Cat# AD 643
Maleimide Cy3B	GE Healthcare	Cat# PA63131
NbALFA	Götzke et al.[60]	N/A
Critical commercial assays		
Human Thrombopoietin Quantikine ELISA Kit	R&D Systems	Cat# DTP00B
Pierce Chromogenic Endotoxin Quant Kit	Thermo Fisher	Cat# A39552
VersaComp Antibody Capture Kit	Beckman Coulter	Cat# B22804
Chromium Next GEM Single Cell 3' Kit v3.1	10x Genomics	Cat# 1000268
Deposited data		
Cryo-EM structure of TPO-2xMPL	RCSB PDB	PDB: 8G04
Cryo-EM map of TPO-2xMPL	EMDB	EMDB: EMD-29644
scRNAseq 10x genomics data	EBI RNA repository	PRJEB61988
Experimental models: Cell lines		
Homo sapiens: HEK293S GnTI$^-$ cells	Reeves et al.[61]	CRL-3022
Homo sapiens: Expi293F cells	Thermo Fisher Scientific	Cat# A14527
Spodoptera frugiperda: Sf9 cells	ATCC	CRL-1711
Homo sapiens: HEK293T	Takara Bio	632180
Homo sapiens: UT7-TPO	Gift from Norio Komatsu (Jichi Medical School, Tochigi, Japan)	N/A
Homo sapiens: HeLa cells	DSMZGerman Collection of Microorganisms and Cell Cultures GmbH	DSMZ No.: ACC 57
Experimental models: Organisms/strains		
Mus musculus: C57BL/6JOlaHsd mice	Envigo	5703F
Recombinant DNA		
pVLAD6	Dukkipati et al.[62]	Addgene Plasmid Cat# 41850
pVLAD6 full-length human MPL	This study	N/A
pVLAD human TPO (residues 22-184) with N-terminal HA signal peptide and FLAG tag	This study	N/A
BestBac 1.0 Linearized Baculovirus DNA	Expression Systems	Cat# 91-001
pD649	ATUM	Cat# PD649

(*Continued on next page*)

Continued

REAGENT or RESOURCE	SOURCE	IDENTIFIER
pD649 full-length human TPO with C-terminal octahistidine tag	This study	N/A
pD649 full-length human TPO with C-terminal octahistidine tag harboring K35A mutation	This study	N/A
pD649 full-length human TPO with C-terminal octahistidine tag harboring K35Q mutation	This study	N/A
pD649 full-length human TPO with C-terminal octahistidine tag harboring R119E mutation	This study	N/A
pD649 full-length mouse TPO with C-terminal octahistidine tag	This study	N/A
pD649 full-length mouse TPO with C-terminal octahistidine tag harboring K35A mutation	This study	N/A
pD649 full-length mouse TPO with C-terminal octahistidine tag harboring K35Q mutation	This study	N/A
pD649 full-length mouse TPO with C-terminal octahistidine tag harboring R119E mutation	This study	N/A
pZEM-hTHPO	Zymogenetics	N/A
pZEM full-length human TPO	This study	N/A
pZEM full-length human TPO harboring R31A mutation	This study	N/A
pZEM full-length human TPO harboring R31E mutation	This study	N/A
pZEM full-length human TPO harboring R31H mutation	This study	N/A
pZEM full-length human TPO harboring R31Q mutation	This study	N/A
pZEM full-length human TPO harboring K35A mutation	This study	N/A
pZEM full-length human TPO harboring K35E mutation	This study	N/A
pZEM full-length human TPO harboring K35H mutation	This study	N/A
pZEM full-length human TPO harboring K35M mutation	This study	N/A
pZEM full-length human TPO harboring K35Q mutation	This study	N/A
pZEM full-length human TPO harboring R38A mutation	This study	N/A
pZEM full-length human TPO harboring R38E mutation	This study	N/A
pZEM full-length human TPO harboring R38H mutation	This study	N/A
pZEM full-length human TPO harboring R38Q mutation	This study	N/A
pZEM full-length human TPO harboring R99A mutation	This study	N/A

(*Continued on next page*)

Continued

REAGENT or RESOURCE	SOURCE	IDENTIFIER
pZEM full-length human TPO harboring R99E mutation	This study	N/A
pZEM full-length human TPO harboring R99H mutation	This study	N/A
pZEM full-length human TPO harboring R99Q mutation	This study	N/A
pZEM full-length human TPO harboring R99W mutation	This study	N/A
pZEM full-length human TPO harboring R119A mutation	This study	N/A
pZEM full-length human TPO harboring R119C mutation	This study	N/A
pZEM full-length human TPO harboring R119E mutation	This study	N/A
pZEM full-length human TPO harboring R119H mutation	This study	N/A
pZEM full-length human TPO harboring R119Q mutation	This study	N/A
pSems leader ALFAtag MPL	This study	N/A
pSems JAK2 (1-827)-mEGFP (Jak2-ΔTK-mEGFP)	https://doi.org/10.1126/science.aaw3242	N/A
pSems-JAK2-(1-543)-mEGFP (Jak2-ΔPKTK-mEGFP)	https://doi.org/10.1126/science.aaw3242	N/A
Software and algorithms		
SerialEM	Mastronarde[63]	http://bio3d.colorado.edu/SerialEM/
Gatan DigitalMicrograph	Gatan	N/A
MotionCor2	Zheng et al.[62]	http://msg.ucsf.edu/em/software/motioncor2.html
cryoSPARC	Punjani. et al.[64]	https://cryosparc.com/download/
Coot 0.9	Emsley and Cowtan[65]	https://www2.mrc-lmb.cam.ac.uk/personal/pemsley/coot/
Phenix suite	Liebschner et al.[66]	https://www.phenix-online.org/
Isolde	Croll[67]	http://isoldehttps//isolde.cimr.cam.ac.uk/
UCSF Chimera 1.14	Pettersen et al.[68]	https://www.cgl.ucsf.edu/chimera/
UCSF ChimeraX 1.6	Pettersen et al.[69]	https://www.rbvi.ucsf.edu/chimerax/
SBGrid	Morin et al.[70]	RRID: SCR_003511
PyMol 2.5.4	Schrödinger	http://www.pymol.org/ ;RRID: SCR_000305
Prism 9	GraphPad	https://www.graphpad.com/
Biacore Insight Evaluation software (v 3.0.12.15655)	Cytiva	Cat# 29310606
PDBsum	EMBL-EBI	https://www.ebi.ac.uk/thornton-srv/databases/pdbsum/Generate.html
SC (Collaborative Computational Project No. 4 : Supported Program)	Lawrence and Colman[71]	https://www.ccp4.ac.uk/html/sc.html
FlowJo software	BD	https://www.flowjo.com/solutions/flowjo
StrataQuest software	Tissuegnostics	https://tissuegnostics.com/products/contextual-image-analysis/strataquest
Fiji ImageJ	NIH, https://doi.org/10.1038/nmeth.2019	https://fiji.sc/
Matlab R2013A and R2018a	MathWorks	RRID: SCR_001622

(*Continued on next page*)

Please cite this article in press as: Tsutsumi et al., Structure of the thrombopoietin-MPL receptor complex is a blueprint for biasing hematopoiesis, Cell (2023), https://doi.org/10.1016/j.cell.2023.07.037

Continued

REAGENT or RESOURCE	SOURCE	IDENTIFIER
Multiple-target tracing algorithm	https://doi.org/10.1038/nmeth.1233	N/A
u-track algorithm	https://doi.org/10.1038/nmeth.1237	N/A
Other		
Anti-FLAG M1 affinity agarose	in-house	N/A
High Affinity Ni-Charged Resin	GenScript	Cat# L00223
Ni-NTA agarose	Qiagen	Cat# 30250
R1.2/1.3 200 gold mesh holey carbon grids	Quantifoil	N/A
Biotin Capture kit, Series S	Cytiva	Cat#28920234

RESOURCE AVAILABILITY

Lead contact

Further information and requests for resources and reagents should be directed to and will be fulfilled by the lead contact, K. Christopher Garcia (kcgarcia@stanford.edu).

Materials availability

All unique/stable reagents generated in this study are available from the lead contact by request.

Data and code availability

- All standardized datasets are publicly available as follows. The cryo-EM map has been deposited in the Electron Microscopy Data Bank (EMDB) under accession code EMD-29644 and the model coordinates have been deposited in the Protein Data Bank (PDB) under accession number 8G04. The scRNAseq 10x genomics data are available under PRJEB61988 via EBI RNA repository.
- All data were analyzed with standard or reported programs and packages, as detailed in the key resources table. This paper does not report original code.
- Any additional information required to reanalyze the data reported in this paper is available from the lead contact upon request.

EXPERIMENTAL MODEL AND STUDY PARTICIPANT DETAILS

Mammalian cell lines and culture conditions

For recombinant production of the TPO-2xMPL complex, suspension HEK293S GnTI$^-$ cells (ATCC CRL-3022) were grown in FreeStyle 293 Expression Medium (Thermo Fisher) supplemented with 1% (v/v) fetal bovine serum (FBS) (Sigma-Aldrich) and maintained at 37°C with 5% CO_2 and gentle agitation. For the production of TPO-containing supernatant, HEK293T cells (Takara Bio) were maintained in Dulbecco's Modified Eagle's Medium (DMEM) supplemented with 2 mM L-glutamine, 10% (v/v) FBS, 1× penicillin/streptomycin (all Gibco) at 37 °C. For cell proliferation and signaling analyses, UT7-TPO cells were maintained in Roswell Park Memorial Institute (RPMI) 1640 medium supplemented with 2 mM L-glutamine, 10% (v/v) FBS, 1× penicillin/streptomycin (all Gibco) and 10 ng/mL recombinant human TPO (gift from Zymogenetics) and cultured at 37°C under 5% CO_2. For TIRF microscopy analysis, HeLa cells were cultivated at 37°C and 5% CO_2 in MEM Eagle medium with EBSS, stable glutamine and 2.2 g/L $NaHCO_3$ (PAN Biotech) supplemented with 10% (v/v) FBS (Merck), non-essential amino acids and HEPES buffer. Umbilical cord blood CD34$^+$ cells were purchased from the Anthony Nolan Trust and stored under liquid nitrogen vapor until use.

Insect cell lines and culture conditions

For BacMam protein expression, baculovirus was produced in *Spodoptera frugiperda* (Sf9) ovarian cells (ATCC CRL-1711) maintained in Sf-900 III medium (Thermo Fisher) with 10% (v/v) FBS (Sigma-Aldrich) and GlutaMAX (Thermo Fisher). Insect cells were grown at 27°C with ambient CO_2 and gentle agitation.

Murine models

Adult male and female wild-type (WT) C57BL/6J (B6) mice of 8-12 weeks were used in all the experiments. All mice were housed under specified pathogen-free conditions at the University of York Biological Services Facility in accordance with FELASA guidelines. All animal procedures were approved by the University of York Animal Welfare and Ethical Review Board and carried out under United Kingdom Home Office license (PPL PP5712003). Mice were randomly assigned to individual experimental groups prior to prebleeding and treatment.

METHOD DETAILS

Preparation of the ligand-receptor complex for structural study

The coding sequences of MPL (UniProt: P40238, residues 1-635) with C-terminal Protein C and octahistidine tags, and N-terminal FLAG-tagged TPO (UniProt: P40225, residues 22-184: TPO_{163}) were each cloned into the BacMam vector pVLAD.[72] We used endogenous signal peptide for MPL and influenza hemagglutinin (HA) signal peptide for TPO (Figure S1A).

P0 viruses were prepared in Sf9 by co-transfecting the expression vector and BestBac Linearized Baculovirus DNA (Expression Systems, CA, USA) using a standard method, and the virus was amplified from P0 to P2. The TPO-MPL complex was produced by co-expression in HEK293S GnTI$^-$ cells using BacMam baculovirus transduction. 3% (v/v) and 7% (v/v) of P2 viruses encoding MPL and TPO, respectively, were added to the cells at a density of 2-3 × 10^6 cells/mL, and the culture flasks were shaken at 37°C for 24 hrs under 5% CO_2. After centrifugation, cells were washed with phosphate-buffered saline (PBS, pH 7.2, Gibco) supplemented with 5 mM EDTA-Na (pH 8.0) and 1:1000 protease inhibitor cocktail (PIC, Sigma Aldrich, MO, USA), weighed and stored at -20°C. The cell pellet was thawed and lysed with a Dounce homogenizer in a lysis buffer composed of 20 mM Tris-HCl pH 8.0, 5 mM EDTA-Na (pH 8.0), and 1:1000 PIC. The lysate was centrifuged at 48,000 *g* for 30 mins, and the membrane pellet was resuspended and nutated for 2 hrs in a solubilization buffer consisting of HBS (10 mM HEPES-Na pH 7.2, 150 mM NaCl), 1% (w/v) Lauryl Maltose Neopentyl Glycol (LMNG, Anatrace; OH, USA), 10% (v/v) glycerol, and cOmplete PIC (Roche, Basel, Switzerland). After centrifugation at 48,000 *g* for 1 hr, 8 mL High Affinity Ni-Charged Resin (GenScript, NJ, USA) was added to the supernatant, and the mixture was incubated at 4 °C for 2 hrs on a rotator. The resin was then collected in a column, washed with HBS containing 0.1% (w/v) LMNG, 0.01 mM TCEP (pH 7.0), and 20 mM imidazole (pH 8.0). The bound protein was eluted in HBS containing 0.1% (w/v) LMNG, 0.01 mM TCEP (pH 7.0), and 250 mM imidazole (pH 8.0) and further purified over an in-house anti-FLAG M1 affinity Sepharose column as follows. The eluate was supplemented with 2 mM $CaCl_2$ before loading over the anti-FLAG M1 affinity column. The column was then washed with wash buffer 1 (HBS with 0.1% (w/v) LMNG, 0.01 mM TCEP (pH 7.0), and 2 mM $CaCl_2$), wash buffer 2 (HBS with 90 mM HEPES-Na pH 8.3, 150 mM KCl, 5 mM ATP, 0.1% (w/v) LMNG, 0.01 mM TCEP (pH 7.0), and 2 mM $CaCl_2$), wash buffer 1, and finally wash buffer 3 (HBS with 0.01% (w/v) LMNG, 0.01 mM TCEP (pH 7.0), and 2 mM $CaCl_2$). The complex was eluted in HBS supplemented with 0.001% (w/v) LMNG, 0.01 mM TCEP (pH 7.0), 0.2 mg/mL FLAG peptide and 5 mM EDTA-Na (pH 8.0), and further purified by size-exclusion chromatography (SEC) using a Superose 6 10/300 column (Cytiva) equilibrated with HBS containing 0.001% (w/v) LMNG and 0.01 mM TCEP (pH 7.0). The SEC-purified sample was concentrated to ~0.2 mg/ml and gently crosslinked with 1 mM bis(sulfosuccinimidyl)suberate (BS3) (Thermo Fisher Scientific, MA, USA) overnight at 4°C, quenched by adding 20 mM Tris-HCl pH 8 and incubation for 30 mins, and re-purified by passing over the Superose 6 10/300 equilibrated in HBS supplemented with 0.001% (w/v) LMNG. The peak fractions containing the crosslinked TPO-2×MPL complex were concentrated to ~3 mg/mL for cryo-EM (Figure S1B).

Cryo-EM sample preparation and data acquisition

0.1 volumes of 0.5% (w/v) digitonin in HBS was added to the concentrated TPO-2×MPL complex in solution, and 3 μL sample was applied onto glow-discharged 200 mesh gold grids (Quantifoil R1.2/1.3). Excess sample was blotted to a filter paper for 3 sec before plunge-freezing using a Leica EM GP (Leica Microsystems) at 8°C and 90% humidity. The grids were initially screened on a Tecnai F20 operated at 200 kV and equipped with a Gatan K2 camera, and the final dataset was collected on a Titan Krios at the CryoEM facility, the HHMI Janelia Research Campus. The microscope was equipped with a Gatan K3 camera and BioQuantum imaging filter and operated at 300 kV in correlated double sampling mode at a nominal magnification of 81,000×, corresponding to the super-resolution pixel size of 0.5039 Å and a calibrated magnification of 46,382×. Each movie was recorded for a total of 6.125 sec with 0.1225 sec exposure per frame at an exposure rate of 9.5 electrons/pixel/second at the sample, that yielded an electron count of ~7.5 electrons/pixel/second at the camera. The datasets were collected using SerialEM software with the defocus range between −0.8 and −2.0 μm and beam-image shift set to collect 9 movies from 9 holes per stage shift with autofocusing.

Cryo-EM data processing

A total of 10,494 movies were subjected to beam-induced motion correction using MotionCor2[62] with binning to a pixel size of 1.078 Å. Dose-weighted motion-corrected micrographs were imported into cryoSPARC,[64] and the patch contrast transfer function (CTF) values were estimated with a default setting. The template-based particle picking was performed using the 2D templates generated from the preliminary 3D map obtained from ab-initio 3D reconstruction followed by non-uniform refinement of selected particles during the screening experiments (Figure S1C). 9,537,683 "particles" were extracted with a box size of 300 pixels and binning to 128 pixels, and two rounds of 2D classifications were performed to remove buffer features and contaminants yielding ~3,358,637 protein particles. Heterogeneous refinements were performed with custom 3D templates to identify a particle set for a more complete extracellular signaling complex (Figure S1E). After further 2D classification, 901,465 selected particles were extracted with a box size of 300 pixels without binning, and repeated heterogeneous 3D refinements and 2D classification yielded 329,658 particles for the final refinement. Iterative local non-uniform refinements with a mask covering the extracellular part and a "center of mask" fulcrum, tilt correction, and per-particle CTF refinements yielded a 3D reconstruction at 3.4 Å resolution as determined by gold-standard Fourier shell correlation (FSC) using the 0.143 criterion. The final map was sharpened with the full map-based

Please cite this article in press as: Tsutsumi et al., Structure of the thrombopoietin-MPL receptor complex is a blueprint for biasing hematopoiesis, Cell (2023), https://doi.org/10.1016/j.cell.2023.07.037

deepEMhancer[73] for overall map representation, and the half map-based Phenix[66] local anisotropic sharpening for model building, visualization of local maps overlaid on the structural model, and real-space refinement. Local resolution was also calculated using Phenix.

Model building and refinement

A homology model for MPL_{CRM1} was generated on the SWISS-MODEL server (swissmodel.expasy.org) using EpoR (PDB: 1EER) as a template. The homology model and the crystal structure of TPO (PDB: 1V7N) were manually placed into the initial cryo-EM density map using UCSF chimera[68] and real-space refined using Phenix.[66] The model was rebuilt and refined iteratively using Coot for manual model building, inspection and correction and ISOLDE[67] in UCSF ChimeraX[69] for molecular dynamics (MD)-based model idealization. MPL_{D4} was replaced with the AlphaFold2 model (AF-P40238-F1), which shows the same chain tracing as the cryo-EM density-based modeling but with a higher quality in the peptide geometry. The structure was rebuilt and refined as described above and further refined using Phenix. The structure and map were visualized using UCSF ChimeraX and PyMol (Schrödinger, LLC). Secondary structure elements were assigned using DSSP.[74] Surface complementary scores were calculated using CCP4 SC.[71]

Preparation and quantitation of TPO variants for screening by cell proliferation and signaling assays

Full-length human TPO (hTPO) variants (R31A, R31E, R31H, R31Q, K35A, K35E, K35H, K35M, K35Q, R38A, R38E, R38H, R38Q, R99A, R99E, R99H, R99Q, R99W, R119A, R119C, R119E, R119H, R119Q) were generated by site-directed mutagenesis using the pZEM-hTHPO plasmid (a gift to Ian Hitchcock from Zymogenetics) as a template and overlapping primers. The presence of the desired mutations was verified using Sanger sequencing (Eurofins Genomics). HEK293T cells (Takara Bio) were maintained in DMEM supplemented with 2 mM L-glutamine, 10% (v/v) FBS, 1× penicillin/streptomycin (P/S; all Gibco) at 37°C under 5% CO_2 and seeded in 6-well plates at a density of 0.5×10^6 cells/well 24 hrs prior to transfection. Cells were transiently transfected with 2 μg pZEM-hTHPO plasmid using jetPRIME transfection reagent (Polyplus Transfections) with a DNA / reagent ratio of 2:1 in the absence of antibiotics. After 72 hrs, supernatants were harvested, concentrated 5-20-fold using 0.5 mL 10k MWCO spin filters (Vivaspin, Satorius) and sterile filtered using 0.22 μm spin filter units (Costar Spin-X). TPO expression was confirmed by western blot using recombinant anti-TPO antibody (ab196026; Abcam). TPO concentrations were quantified using Human Thrombopoietin Quantikine ELISA Kit (R&D Systems) according to manufacturer's instructions after 1:500 dilution of conditioned supernatants in DMEM supplemented with 10 % (v/v) FBS. For long term storage, concentrated supernatants were stored at -80°C and working stocks were kept at 4°C.

Cell Proliferation assays

UT7-TPO cells were maintained in RPMI 1640 medium supplemented with 2 mM L-glutamine, 10% (v/v) FBS, 1× P/S and 10 ng/mL recombinant human TPO (rhTPO, Zymogenetics) and cultured at 37°C under 5% CO_2. 16 hrs prior to starting proliferation assays, UT7-TPO cells were washed twice with PBS and plated in starvation media (RPMI 1640 medium supplemented with 2 mM L-glutamine, 2% (v/v) FBS and 1× P/S, but without rhTPO). TPO supernatants were diluted in starvation media. 30 μL UT7-TPO cells at 9×10^4 cells/mL were then seeded in 384-well plates (Greiner) and incubated at 37°C in the presence of increasing concentrations (10^{-2} to 10^2 ng/mL) of TPO^{mod} supernatant. After 72 hrs, cells were incubated for 4 hrs with CyQUANT XTT reagent (Invitrogen) and absorbance was read at 450 nm and 660 nm on a FLUOstar Omega microplate reader (BMG Labtech). Absorbance values from cells treated with supernatant from a no-template control transfection were subtracted from all samples and cell growth was plotted relative to cells grown in the absence of TPO.

Multiplex fluorescent barcoding and phospho-flow cytometry

1×10^5 UT7-TPO cells were seeded in each well of a 96-well V bottom plate (Greiner). For TPO titrations, cells were stimulated with 0 to 100 ng/mL of TPO^{mod} supernatant at 37°C for 30 mins. For TPO kinetic assays, cells were stimulated with 50 ng/mL of each mutant TPO supernatant at 37°C for 0 to 240 mins. In all experiments, stimulation was stopped by fixing cells for 15 mins with 2% paraformaldehyde (PFA) while shaking at RT. Cells were washed and pellets resuspended in 200 μL ice-cold methanol for at least 30 mins at -20°C or for up to 2 weeks at -80°C. Following permeabilization, cells were washed once with FACS buffer (PBS, pH 7.4, supplemented with 1% (w/v) bovine serum albumin (BSA) and 0.05% (v/v) sodium azide) then once with PBS, pH7.4, prior to barcode labelling. Briefly, DyLight800 NHS Ester (Thermo Scientific) and Pacific Blue Succinimidyl Ester (Thermo Scientific) dyes were diluted in DMSO to 100 μg/mL and then separately serially diluted 2-fold to achieve the lowest concentration of 0.4 μg/mL. 16 unique dye combinations were created by mixing 0, 3.13, 12.5 and 50 μg/mL stocks from the serial dilution in a 1:1 ratio. 4 μL of each dye mix was added to wells followed by 200 μL PBS, pH 7.4, to re-adjust pH to neutral. Cells were incubated in the dark on a plate shaker at 4°C for 40 mins. Cells were washed twice with FACS buffer and each combination of 16 barcodes was pooled, washed and stained with Fc block (human TruStain FX, Biolegend) for 10 mins at 4°C. Each well was topped up with 100 μL FACS buffer and split across nine wells of a 96-well V-bottom plate. Cells were pelleted and pellets were washed before resuspension in the relevant antibody mix and incubated with shaking in the dark at RT for 1 hr. Cells were washed twice with FACS buffer and analyzed on a CytoFlex LX flow cytometer (Beckman Coulter) and data analyzed using FlowJo software (BD).

Purification of TPO variants for signaling and functional analyses

Full-length mature sequences of WT and mutant (K35A, K35Q, or R119E) hTPO and murine Tpo (mTPO) were cloned into pD649 (ATUM)[75] with an N-terminal HA signal peptide and C-terminal octahistidine tag, and the proteins were expressed using the Expi293 expression system (Thermo Fisher Scientific). Expi293 cells were maintained in Expi293 Expression Medium at a density between 0.3 × 10^6 cells/mL and 6 × 10^6 cells/mL at 37°C under 5% CO_2, and transfection was performed at a density of 3 × 10^6 cells/mL. One day after transfection, enhancers included in the ExpiFectamine 293 Transfection Kit (Thermo Fisher Scientific) were added to the culture according to the manufacturer's protocol and the protein was expressed for 72 hrs at 37°C under 5% CO_2 or at 32°C with ambient CO_2. At 37°C, mTPO yielded substantially more misfolded proteins than hTPO, and mTPO required expression at lower temperatures to alleviate this aggregation. 30°C with 5% CO_2 yielded a comparable amount of active mTPO protein to 32°C without added CO_2. The supernatant was collected and diluted with 1.5 volumes of PBS pH 7.2 containing 10 mM Tris-HCl pH 8.0 and His-tagged TPO was purified using Ni-NTA agarose (Qiagen). After washing the resin, bound proteins were eluted in PBS pH 7.2 supplemented with 200 mM imidazole (pH 8.0), and the eluted proteins were further purified by SEC using a Superdex 200 10/300 (Cytiva) equilibrated with PBS pH 7.2 containing 2 mM EDTA-Na (pH 8.0). Proteins were concentrated, and the mTPO variants were passed through Pierce High Capacity Endotoxin Removal Spin Columns (Thermo Fisher). Endotoxin levels were quantitated with Pierce Chromogenic Endotoxin Quant Kit (Thermo Fisher). Protein concentrations were determined using UV absorbance at 280 nm.

Surface Plasmon Resonance Analysis

Surface plasmon resonance (SPR) experiments were performed using a Biacore T200 (Cytiva, Uppsala, Sweden) with the sample compartment at 15°C and an analysis temperature of 25°C. Purified biotinylated ectodomain of the human MPL (amino acids 26-491) carrying a C-terminal Avi-His tag (MPL-ECDbio) was a gift from Cancer Research Horizons (Stuart Haynes, Stephanie Ryman). Purified full-length human TPO carrying a C-terminal 8×His tag was prepared as described above. The SPR assay was configured in such a way as to measure high affinity (site 1) binding of MPL to TPO (Figure S5B). Attempts to develop an SPR assay to measure site 2 binding of MPL to TPO were unsuccessful for multiple technical reasons.

MPL-ECDbio was captured on the surface of a Series S sensor chip CAP using a Biotin CAPture kit according to the manufacturer's instructions (Cytiva, Uppsala, Sweden). For kinetic experiments, a capture level of ~30-40 response units was used. The reference flow cell comprised Biotin CAPture reagent. The chip was prepared, TPO dilutions were made up and binding experiments were run in 1× HBS-EP+ buffer [10 mM HEPES-Na, pH 7.4, 150 mM NaCl, 3 mM EDTA, 0.05% surfactant P20 (Cytiva, Uppsala, Sweden)]. Molar TPO concentrations were determined from the absorbance at 280 nm which was measured in triplicate using a NanoDrop2000 spectrophotometer (Thermo Scientific) and an extinction coefficient of 17210 M^{-1} cm^{-1}. TPO stock solutions (in PBS, pH 7.2, supplemented with 2 mM EDTA) were diluted in three steps: in the first step, a 10× stock was prepared, in a second step the 10× stock was diluted to provide 0.32 mL of the highest concentration to be used in the assay (1× stock), in the third step a 3-fold serial dilution was made from the 1× stock. For multicycle kinetic experiments, six increasing concentrations of TPO were injected over the reference and MPL-ECDbio flow cells at a flow rate of 50 μL/min for 120 sec, followed by a dissociation phase of 600 sec. The surface was then washed with 10 mM HEPES-Na, pH 7.4, 500 mM NaCl, 3 mM EDTA, 0.05% surfactant P20 (100 sec at 10 μL/min). For each concentration series, the fourth dilution was injected in duplicate and buffer injections were included before and after each series. Two independent experiments were carried out. Data were analyzed using Biacore Insight Evaluation software (v 3.0.12.15655) by fitting to a 1:1 binding model with fixed, constant refractive index. Data were also analyzed by fitting to a steady state affinity model. Average dissociation constant (K_{D1}) for site 1 binding of each TPO variant to immobilized MPL was calculated using the KD values derived from the kinetic and steady state affinity fits, and values for TPO^{mod} were compared to WT TPO by application of a paired two-tailed Student's t-test.

Mouse TPO treatment

Male and female wild-type (WT) C57BL/6J (B6) mice of 8-12 weeks were used in all the experiments. Blood samples from the saphenous vein were collected in EDTA tubes and complete blood counts (CBCs) were analyzed using a ProCyte Dx Hematology Analyzer (IDEXX). Baseline blood counts were determined 72 hrs prior to treatment with recombinant mTPO. Mice were intraperitoneally injected with either sterile PBS, pH 7.4 or 5 μg mTPO (WT or TPO^{mod}) diluted in sterile PBS, pH 7.4, daily for five days and CBCs were assessed on days 5 and 7. Mice were euthanized on day 7 post-treatment by CO_2 asphyxiation and cervical dislocation, and femurs were harvested for flow cytometry and histological analysis. To determine normalization of CBCs, a subset of mice from each treatment group were monitored and bled on days 10 and 14. All mice were housed under specified pathogen-free conditions at the University of York Biological Services Facility. All animal procedures were approved by the University of York Animal Welfare and Ethical Review Board and carried out under United Kingdom Home Office license (PPL PP5712003).

Flow cytometry analysis of hematopoietic stem cells (HSCs) and megakaryocyte progenitors (MKPs) in mouse bone marrow

Bone marrow was harvested from one femur. Red blood cell lysis was performed using 140 mM Tris-ammonium chloride, pH 7.2, at room temperature for 5 mins prior to washing with PBS, pH 7.4, and centrifugation at 300 *g*. The resulting pellet was stained for specific markers to analyze HSCs and progenitors. Reagents and optimized antibody dilutions are presented in key resources table.

Staining was performed for a total of 45 mins at 4°C including a 15 min incubation with Zombie Aqua (Biolegend) for live/dead separation. After washing in PBS, pH 7.4, the samples were centrifuged at 300 *g* for 10 mins, resuspended in PBS, pH 7.4, with 2 mM EDTA and 5% (v/v) FBS and analyzed using a Cytoflex LX (Beckman Coulter). All single-stained controls were stained using VersaComp Antibody Capture Kit (Beckman Coulter) according to the manufacturer's instructions. Cells were analyzed on a CytoFlex LX flow cytometer (Beckman Coulter) and data analyzed using FlowJo software (BD).

Histological analysis of mouse bone marrow

To perform immunohistological analysis of the bone marrow, harvested femurs were fixed overnight in 4% (v/v) PFA, decalcified for two days in PBS, pH 7.4, 10% (w/v) EDTA and finally fixed in optimum cutting temperature compound (OCT; CellPath) following an overnight incubation in 20% (w/v) sucrose in PBS, pH 7.4. 8 μm-thick sections were cut using a cryostat (Leica CM1950) and stored at -20°C prior to treatment with ice-cold acetone for 5 minutes. All subsequent steps were performed at room temperature, and PBS, pH 7.4, containing 0.05% (w/v) BSA was used to wash the sections and dilute reagents. Sections were washed and blocked with 5% (v/v) rat serum for 30 mins. Following two washes, the sections were then blocked with ReadyProbes Avidin/Biotin Blocking Solution (Invitrogen) according to the manufacturer's protocol. The sections were washed and incubated for 1 hour with a primary antibody against CD41 (Invitrogen, 13-0411-85) or an isotype control (Biolegend, 400403) (1:200). Following three washes, the sections were incubated with Streptavidin AF546 (Invitrogen, S11225) for 45 mins. After three washes, an additional wash in PBS, pH 7.4, without BSA was followed by nuclear staining with DAPI (1 μg/mL) (Biolegend). The sections were washed twice in PBS and mounted using Prolong Gold (Invitrogen). Whole BM sections were imaged using a Axio Scan.Z1 slide scanner (Zeiss) and analyzed using StrataQuest software (Tissuegnostics).

Umbilical cord blood (UCB) CD34 cell culture and signaling

$CD34^+$ cells were obtained from the Anthony Nolan Trust. Cells from four independent UCB donors were mixed, and 2×10^4 cells were cultured in triplicate or quadruplicate in StemSpan SFEM II (STEMCELL Technologies) supplemented with 150 ng/mL stem cell factor (SCF) and 150 ng/mL Flt3L (both Biolegend). Commercial hTPO at 20 ng/mL (1 nM, residue 22-195, Peprotech) was used as a control, and compared to full length recombinant human TPO variants (WT or TPO^{mod}) at 20 ng/mL (0.5 nM) or 40 ng/mL (1 nM). After seven days of culture, half of the samples were re-treated with fresh TPO variants for one hour. All samples were incubated with DAPI (Thermo Fisher) for 15 mins, washed in PBS, pH 7.4 and centrifuged at 300 *g* for 10 mins at 4°C. The pellets were resuspended and fixed in 4% (v/v) PFA in PBS, pH 7.4, for 15 mins and washed in PBS after addition of 50 μL of Precision Count Beads (Biolegend). Cells were permeabilized by incubation in ice-cold methanol for 40 mins at -20°C. Fixed cells were washed in PBS supplemented with 2% (v/v) FBS, and staining was performed using the antibody panels detailed in key resources table for 30 mins on ice.[48,76,77] The samples were then washed in PBS, pH 7.4, and centrifuged at 300 *g* for 10 mins prior to analysis. All single-stained controls, except DAPI, were stained using VersaComp Antibody Capture Kit (Beckman Coulter) according to the manufacturer's instructions. Cells were analyzed on a CytoFlex LX flow cytometer (Beckman Coulter) and data analyzed using FlowJo software (BD).

Single cell RNA sequencing library preparation

Single cell 3′ mRNA sequencing libraries were prepared using the 10X Genomics Chromium system, with the Chromium Next GEM 3' single cell reagent kit v3.1 (dual index). Approximately 16,500 live, freshly isolated and counted $CD34^+$ $CD45RA^-$ cells per sample were loaded onto individual lanes of a Chromium chip G, with the aim of recovering 10,000 cells per sample for cDNA synthesis and library preparation, performed according to the manufacturer's guidelines. Barcoded libraries from all four samples were pooled and sequenced on an Illumina NextSeq2000 instrument at the University of Leeds Next Generation Sequencing Facility, with a P3 high output 100 cycle sequencing kit (Read 1 = 28 nt, Index 1 = 10 nt, Index 2 = 10 nt, Read 2 = 90 nt). Demultiplexing and BCL to fastq conversion was performed using 10X Genomics Cellranger software (mkfastq protocol). Data analysis was performed using Seurat, Monocle and UCell packages.

Single molecule fluorescence imaging and analysis

Prior to microscopy experiments, confluent HeLa cells were trypsinized, transferred to a 60 mm cell culture dish and transiently transfected via calcium phosphate precipitation.[78] Transfected cells were seeded onto 25 mm glass coverslips coated with a poly-L-lysine-graft (polyethylene glycol) copolymer functionalized with RGD to minimize non-specific binding of fluorescent NBs.[79]

Receptor dimerization in the plasma membrane of living cells was quantified by dual-color single molecule FRET localization and tracking as described previously.[27] Dimerization experiments were performed in HeLa cells transiently expressing JAK2ΔTK or JAK2ΔPKΔTK C-terminally fused to mEGFP and MPL N-terminally fused to the ALFA-tag. Cell surface receptors were labeled via ALFA-tag nanobodies (NbALFA),[60] which were site-specifically conjugated with a fluorophore via an additional C-terminal cysteine residue by using maleimide chemistry. Imaging experiments were carried out 24 hrs post transfection at 25 °C in medium without phenol red and supplemented with an oxygen scavenger and redox-active photoprotectant to minimize photobleaching.[80] For cell surface labeling of ALFA-tagged receptors, a mixture of NbALFA conjugated to Cy3B and ATTO643, respectively, were added to the medium at equal concentrations (2.5 nM each) and kept in the medium during the experiment. After incubation with TPO variants for 5 min, single molecule FRET time-lapse imaging was carried out by TIRF microscopy with sequential excitation at 561 nm and 642 nm for 25 msec per channel, resulting in an overall frame rate of 20 frames per second (fps). Before image acquisition,

co-expression of JAK2ΔTK or JAK2ΔPKΔTK was confirmed by mEGFP fluorescence upon excitation at 488 nm. Images were acquired by an EMCCD camera (iXon Ultra, Andor) using an image splitter (QuadView, Photometrics). Alternating laser excitation was achieved with a simple micro-controller (Arduino Uno) and open-source acquisition software[81] synchronizing laser shuttering via an AOTF (AA.AOTFnC-400.650-TN, AA Opto Electronic) and camera triggering.

Lifetimes of WT TPO- or TPO^{mod}-induced MPL dimers were estimated in the presence of JAK2ΔPKΔTK, in which the dimers were not stabilized by JAK2 PK-PK interactions. However, we note that although the apparent dimer lifetime induced by WT TPO is 0.88 sec, we did not observe significant association and dissociation events, and most of the receptors were dimerized for the whole experiment such that the observed decay was caused by the tracking fidelity. However, for the TPO^{mod} variants, we could see more dynamic events, therefore the reduced lifetime as compared to WT TPO can be interpreted as reduced complex stability.

Single molecule image analysis was carried out using self-written MATLAB code "SLIMfast" as described previously.[27] Single molecules were localized using the multiple-target tracing algorithm[82] and receptor dimerization was quantified based on localizations in the sensitized acceptor fluorescence channel relative to the cell surface receptor density obtained from donor and acceptor channels. FRET efficiencies E were determined from the changes in donor intensity before (I_{DA}) and after (I_D) acceptor bleaching[27]:

$$E = 1 - \frac{I_{DA}}{I_D}$$

Distances were calculated from FRET efficiencies assuming a Förster radius of 6.4 nm:

$$E(r) = \frac{R_0^6}{R_0^6 + r^6}$$

QUANTIFICATION AND STATISTICAL ANALYSIS

All quantitative data from *in vivo* and *in vitro* cellular experiments were analyzed in GraphPad Prism smFRET data were analyzed with MATLAB. All scRNAseq data were analyzed using the Seurat, Monocle 3 and UCell packages. All surface plasmon resonance data were analyzed using the Biacore Insight software with technical and experimental replicates as specified in the STAR Methods. Affinity data from individual SPR experiments were aggregated using Microsoft Excel. "n" represents the number of biological replicates from independent animal, human or cell culture sources. All n, statistical tests and P values are detailed in figures, tables, and figure and table legends.

CellPress
OPEN ACCESS

Supplemental figures

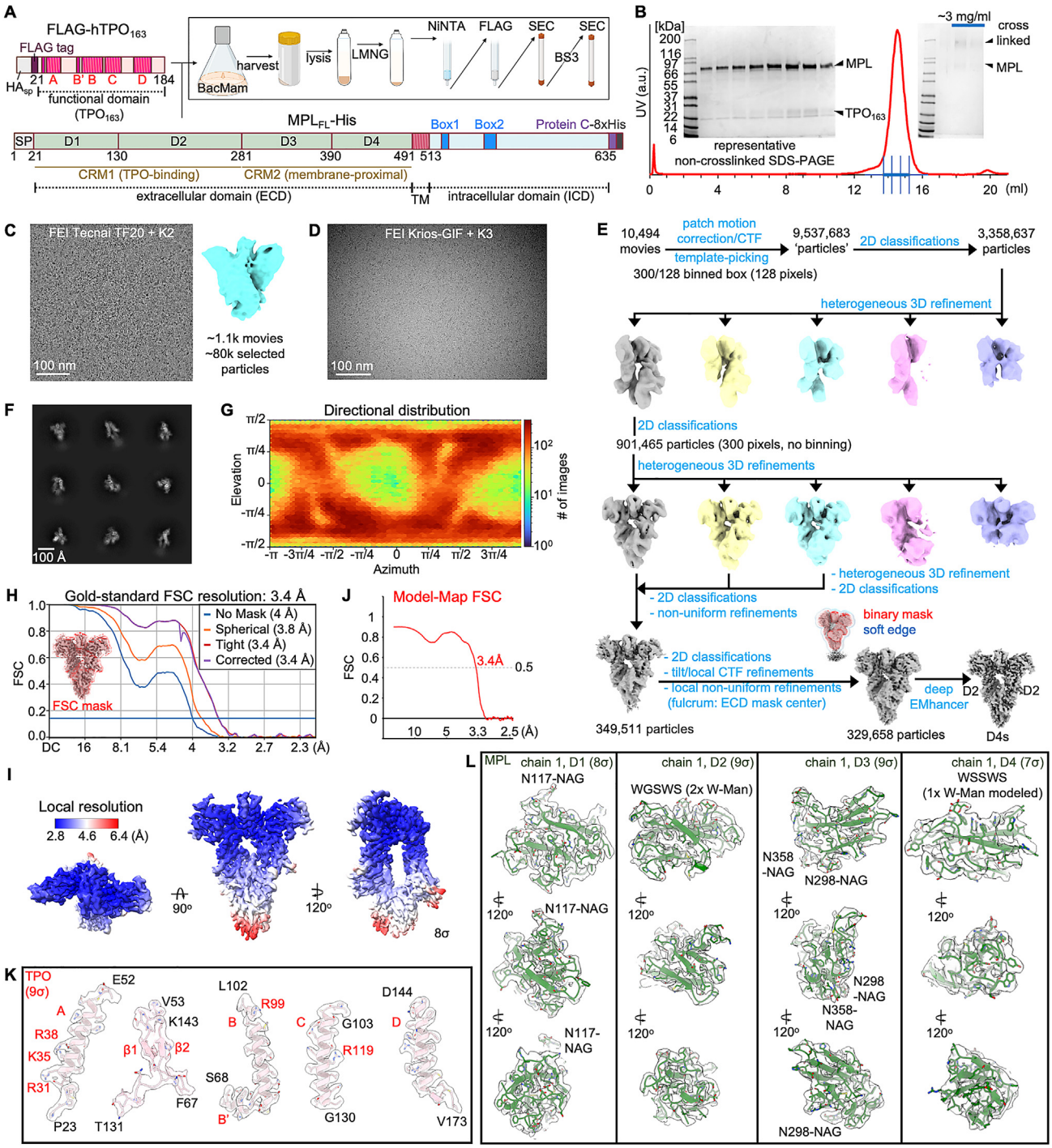

Figure S1. Purification and cryo-EM of the TPO-2×MPL complex, related to Figure 1

(A) Schematic of the recombinant expression constructs for TPO and MPL with purification scheme for structural study.

(B) Representative final SEC profile and SDS-PAGE.

(C) A preliminary cryo-EM micrograph and 3D reconstruction from initial screening experiments.

(D) Representative cryo-EM micrograph.

(legend continued on next page)

(E) Cryo-EM data processing scheme used to generate the 3D reconstruction of TPO-2×MPL_{ECD}.
(F) Representative 2D class averages from the final particle sets.
(G) Orientation distribution of the aligned particles in the final 3D reconstruction output from cryoSPARC.
(H) Gold-standard Fourier shell correlation (FSC) curves for the final 3D reconstruction. The FSC mask (red) for the corrected FSC curve is overlaid onto the 3D map of TPO-2×MPL_{ECD} (gray).
(I) Local resolution estimates from Phenix, colored on the surface representation of the deepEMhancer sharpened map. Blue, white and red correspond to 2.8, 4.6 and 6.4 Å, respectively. The map contour level is set to 8σ.
(J) Map-model FSC correlation calculated by Phenix.
(K and L) Local cryo-EM maps overlaid on (K) the segmented TPO structure or (L) D1, D2, D3, and D4 of MPL. The map contour levels are indicated in the figure panels.

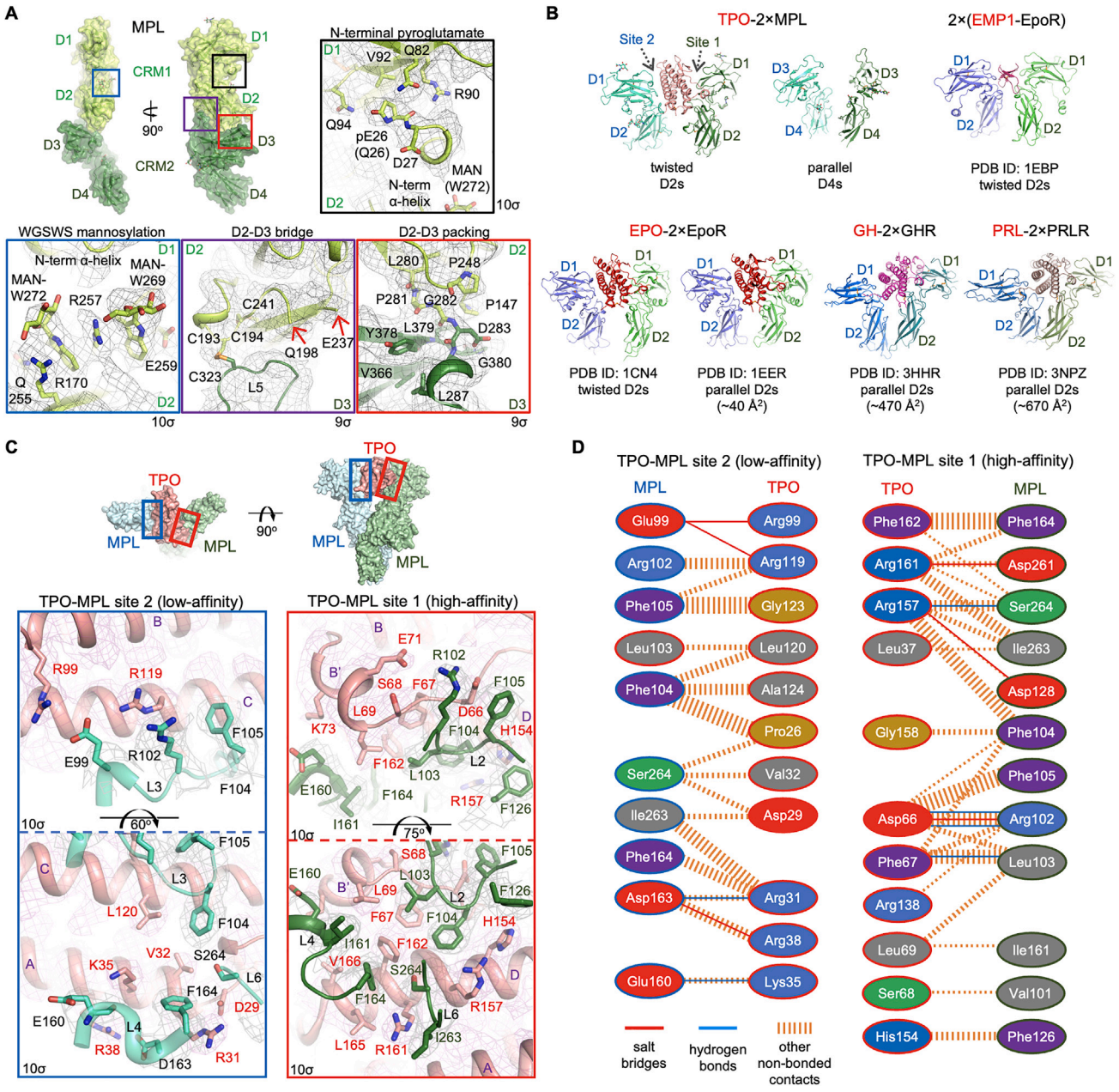

Figure S2. Structural characteristics of the TPO-2×MPL complex, related to Figure 2

(A) Structural features of the extracellular region of MPL with cryo-EM map. A surface representation of MPL chain 1 is colored lime for CRM1 and dark green for CRM2 and zoomed-in boxes are indicated. The boxed regions are magnified and displayed in ribbon and stick models with black-mesh cryo-EM density overlayed at the contour level of 9σ. Black box, N-terminal pyroglutamate and surrounding structure; blue box, tryptophan mannosylation on the WGSWS motif, purple box, disulfide bond bridging D2 and D3; red box, domain packing between D2 and D3.

(B) Cartoon models showing the structural comparison of the relative CRM geometries among the GHR family. Buried surface area between contacting D2 domains is indicated in parentheses.

(C) Magnified views of the site 1 and 2 TPO-MPL interfaces with cryo-EM map contoured at 9σ. The views correspond to those shown in Figure 2B.

(D) The interaction diagram for the TPO-2×MPL complex at the site 1 (right) and site 2 (left) interfaces created using PDBsum (ebi.ac.uk/pdbsum). The cartoons are colored in blue (positively charged amino acids; His, Lys, and Arg), red (negatively charged; Asp, Glu), green (neutral polar; Ser, Thr, Asn, Gln), yellow (Cys), gray (aromatic; Phe, Tyr, Trp), purple (aliphatic; Ala, Val, Leu, Ile, Met), and orange (Pro and Gly).

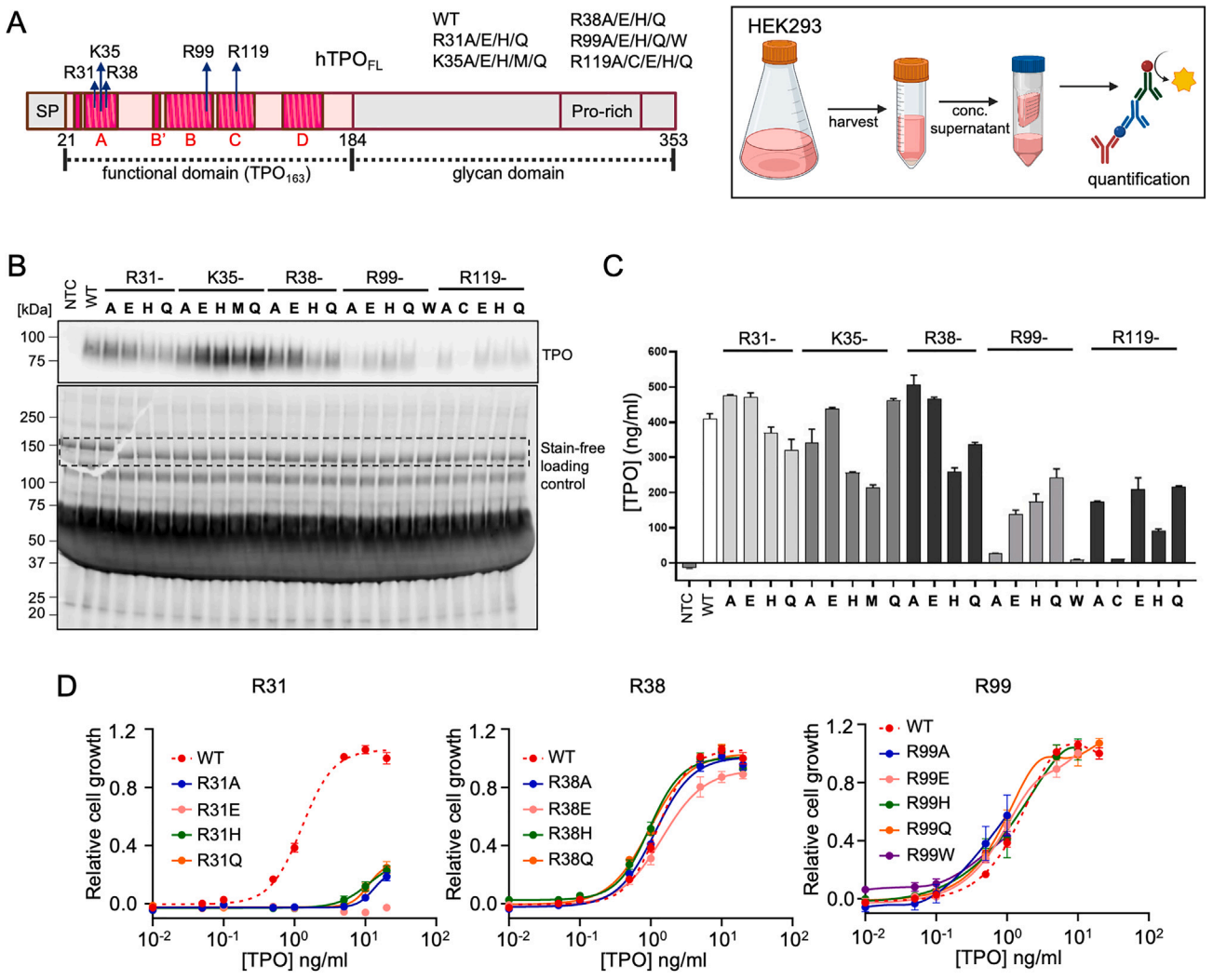

Figure S3. Preparation of human TPO variants and assessment of their ability to support UT7-TPO cell growth, related to Figure 3

(A) Domain diagram of full-length human TPO with sites of mutagenesis indicated with arrows, and introduced mutations tabulated to the right (left); expression, preparation and quantification scheme (right). TPO variants were used without purification for the cell growth assays.

(B) Representative SDS-PAGE (lower) and anti-TPO immunoblot (upper) analysis showing levels of TPO expression in cell-free supernatants. Equal supernatant volumes were loaded per lane.

(C) Quantification of TPO expression levels by ELISA.

(D) UT7-TPO cell proliferation data for TPO variants measured using an XTT assay after 72 h.

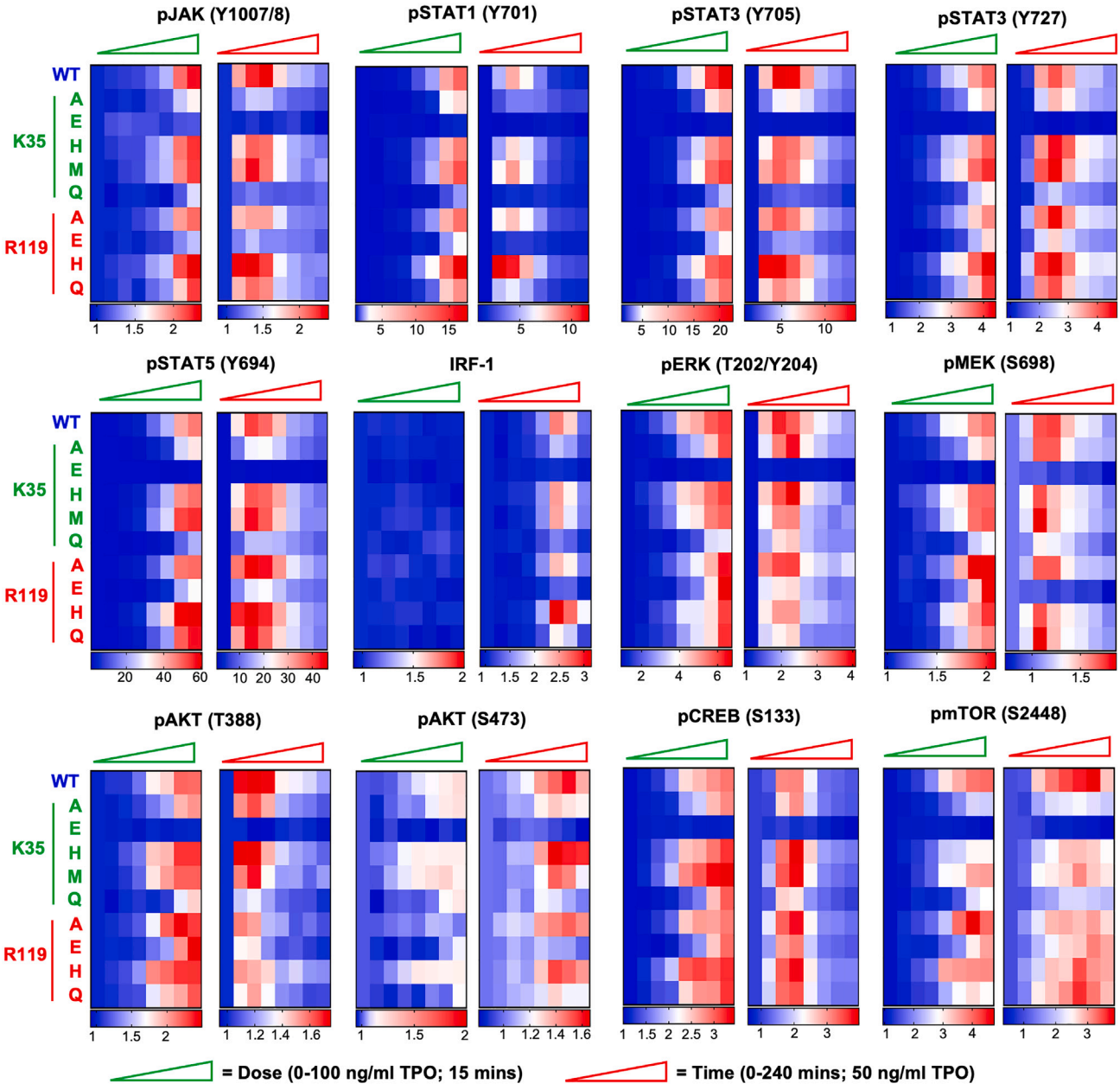

Figure S4. Dose response and kinetics signaling assays for TPO K35 and R119 variants in UT7-TPO cell cultures, related to Figure 3

For the dose response signaling assays, UT7-TPO cells were treated with cell-free supernatants containing WT TPO, TPO-K35, or TPO-R119 variants at the indicated concentrations. Phosphorylation of downstream effectors in fixed cells after 30 min was measured using barcode-labeled phosphoflow cytometry. For the signaling kinetics assays, UT7-TPO cells were treated with cell-free supernatants containing 50 ng/mL WT TPO, TPO-K35, or TPO-R119 variants for the indicated times. Phosphorylation of downstream effectors in fixed cells was measured using barcode-labeled phosphoflow cytometry. Heatmaps represent mean fold-change in median fluorescent intensity (MFI; n = 3) compared to unstimulated.

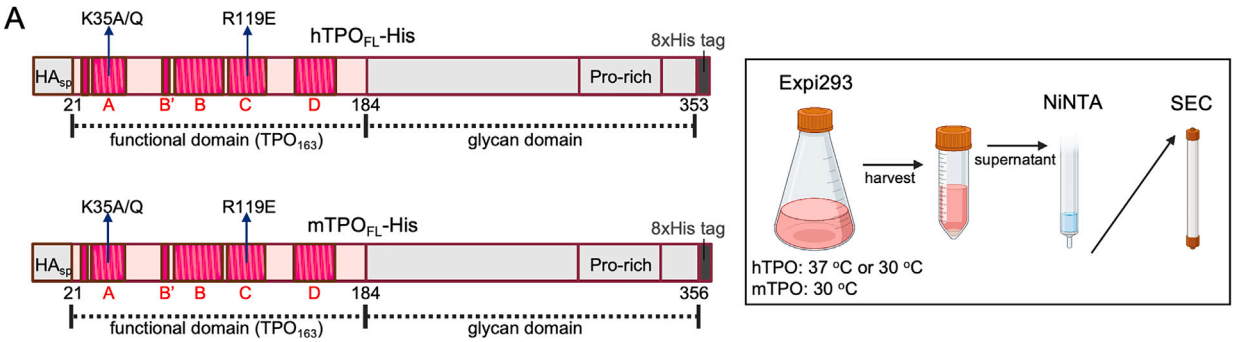

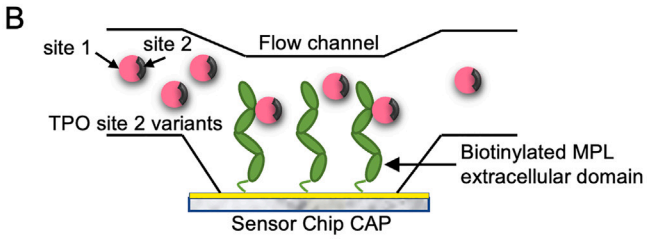

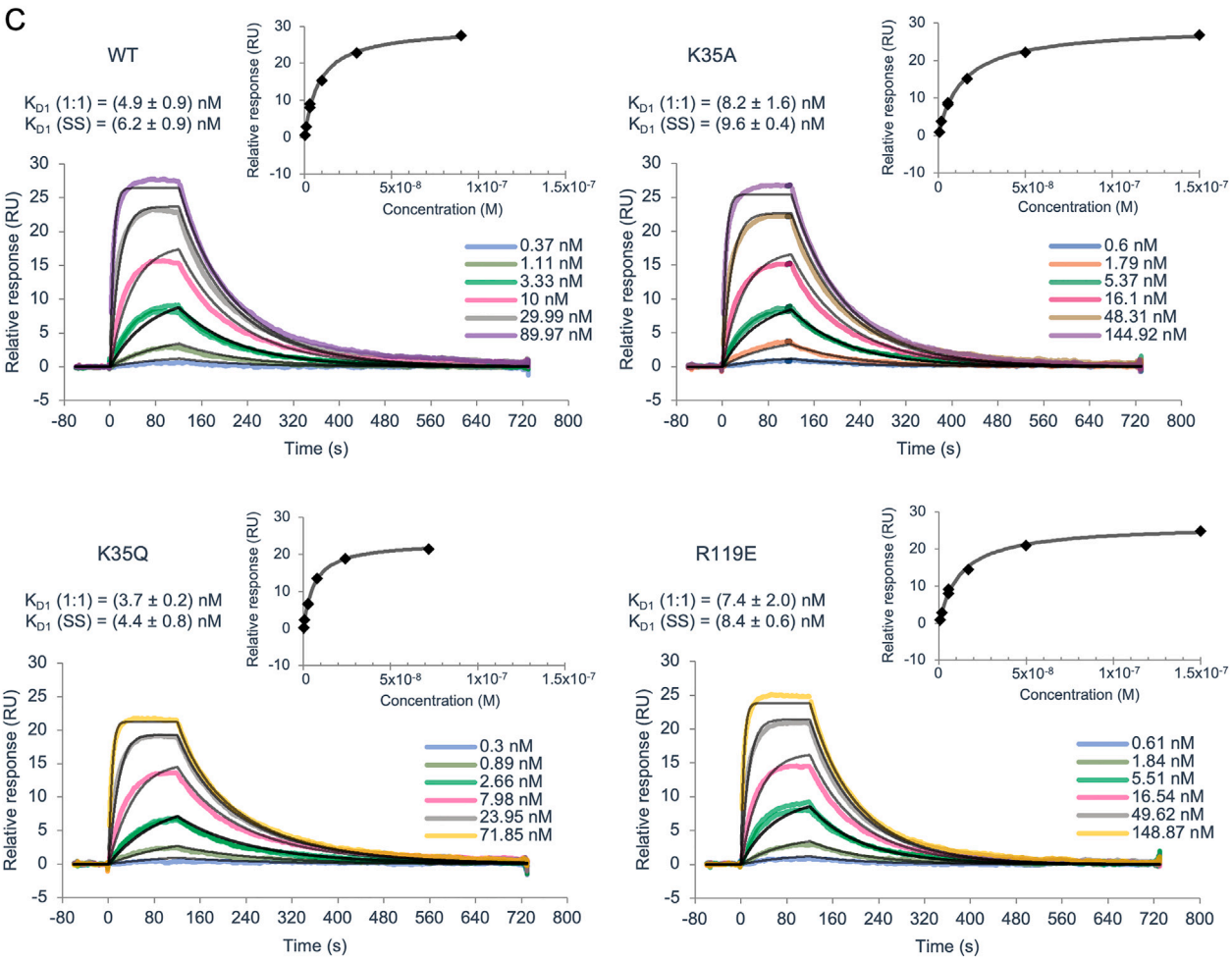

(legend on next page)

Figure S5. Purification of full-length human TPO variants and assessment of their ability to bind to MPL via the high-affinity site 1 using surface plasmon resonance (SPR), related to Figures 3, 4, and 5

(A) Domain diagrams of the C-terminal 8×His-tagged full-length human and murine thrombopoietin, and schematic of their expression and purification. The mutagenesis sites and the introduced mutations are indicated in the figure panel.

(B and C) (B) Schematic and (C) representative sensorgrams of SPR experiments. (B) High-affinity (site 1) binding of TPO to MPL was examined. MPL extracellular domain (26–491) was captured on the chip surface via a biotinylated Avi-tag and recombinant full-length TPO was injected over the chip as analyte. (C) Representative multicycle kinetics sensorgrams are shown for WT TPO and three TPO^{mod} (K35A, K35Q, R119E) (colored lines, TPO concentrations shown in the inset legend) binding to MPL and are overlaid with their fit to a 1:1 interaction model (black line). Inset shows corresponding steady-state affinity fit. RUs, response units. Average K_{D1} ± SD derived from the kinetic fit (1:1) and steady-state (SS) fit are reported for each TPO variant above the relevant sensorgram plot.

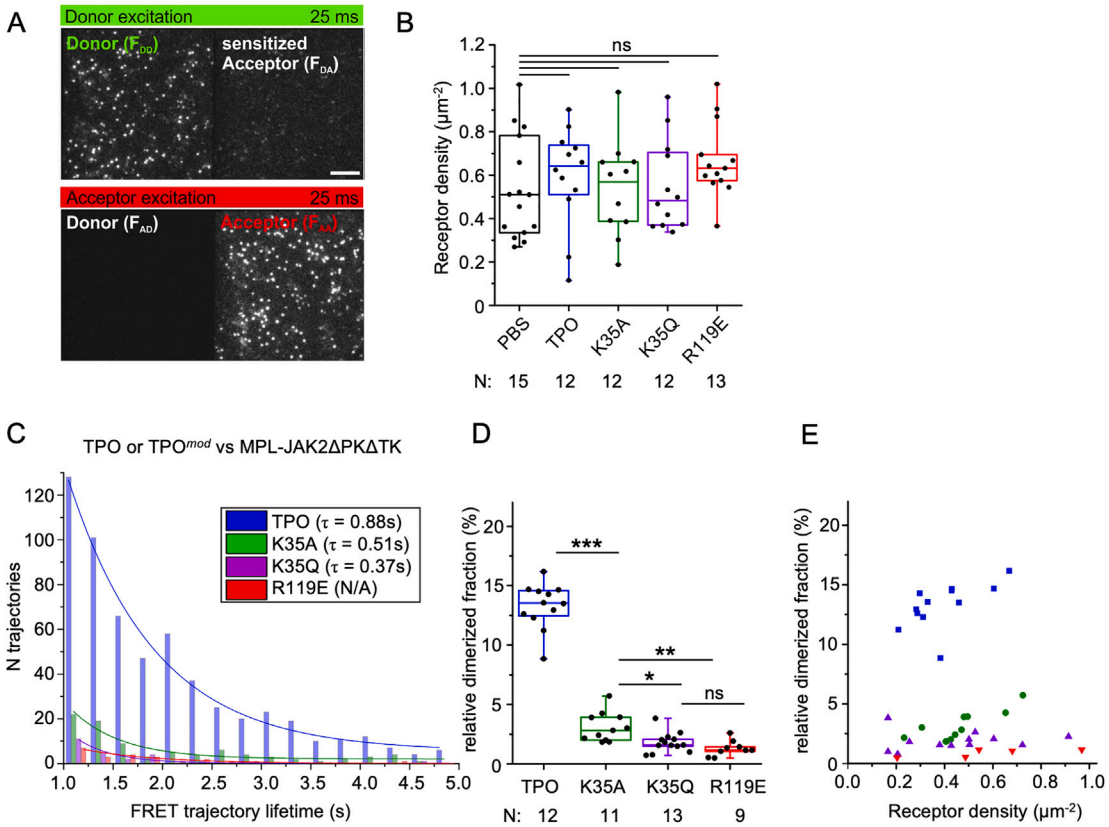

Figure S6. Cell-surface MPL dimerization detected by single-molecule FRET, related to Figure 4

(A) Experimental workflow for single-molecule FRET detection by alternating laser excitation. Scale bar is 5 μm.

(B) Comparison of the MPL density observed in the corresponding cells (Figure 4C) in the presence of JAK2ΔTK.

(C) Lifetimes estimated from tracked FRET signals of MPL complexes dimerized by WT TPO or TPO^{mod} in the presence of JAK2ΔPKΔTK (JAK2 FERM-SH2 domain). TPO^{mod} show reduced receptor complex lifetime compared to TPO (τ_{TPO} = 0.88 s, τ_{K35A} = 0.51 s, τ_{K35Q} = 0.37 s). Each histogram represents the pooled trajectories (TPO: 12 cells, K35A: 11 cells, K35Q: 13 cells, R119E: 9 cells).

(D) Quantification of MPL-JAK2ΔPKΔTK homodimerization in the presence of TPO^{mod}. Each data point represents the analysis from one cell.

(E) Plots of the MPL-JAK2ΔPKΔTK homodimerization versus overall receptor densities. Data in (B) and (D) are presented as box plots and indicate the data distribution of 2nd and 3rd quartile (box), median (line) and minimum and maximum values (whiskers). Each data point represents the analysis from one cell with the number (N) of cells measured for each condition indicated. Significances were determined using the two-sample Kolmogorov-Smirnov test in MATLAB. *p ≤ 0.05; **p ≤ 0.01; ***p ≤ 0.001; ns, not significant.

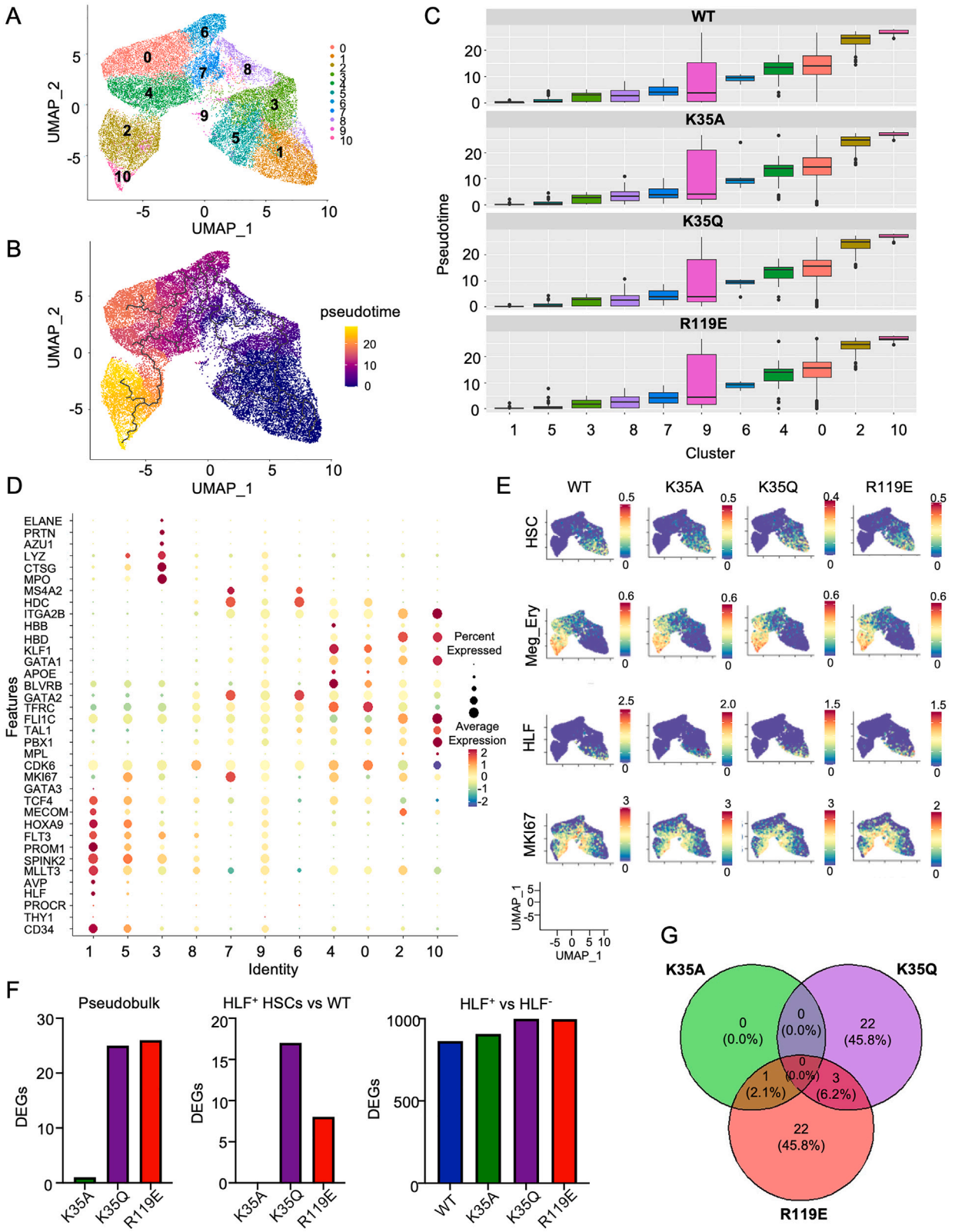

(legend on next page)

Figure S7. Dimensionality reduction, pseudotime mapping, and identification of HSCs and differentially expressed genes in scRNA sequencing (scRNA-seq), related to Figure 6

(A) Merged UMAP clustering of all scRNA-seq data.

(B and C) (B) Pseudotime projection on UMAP and (C) across clusters for WT and TPO^{mod}.

(D) Features distinguishing clusters to identify HSCs and downstream progenitors from pseudotime.

(E) Expression of HSC genes, Megakaryoctye/Erythroid progenitor genes, *HLF* and *Ki67* across UMAP clusters.

(F) Number of differentially expressed genes between WT and TPO^{mod} in pseudobulk, *HLF*$^{+}$ HSCs and *HLF*$^{+}$ vs. *HLF*$^{-}$ cells.

(G) Venn overlap of pseudobulk differentially expressed genes between WT and TPO^{mod}.